E-741

INCLUSIVE CENTRAL JET PRODUCTION AT $\sqrt{s} = 1.8$ TEV

A Thesis

Submitted to the Faculty

of

Purdue University

by

Stephen Eugene Kuhlmann

In Partial Fulfillment of the

Requirements for the Degree

Doctor of Philosophy

August 1988

ACKNOWLEDGMENTS

I wish to acknowledge the support I have received during my graduate studies. I thank my wife Roxy for her infinite patience and support. I also thank my family for their support. I thank my advisor Art Garfinkel for his endless source of ideas and enthusiasm. I also want to thank Steve Behrends and John Huth for their immeasurable help during the later stages of the analysis, Rick St. Denis for teaching me how to get out of bed at 4 a.m., Lou Dalmonte and Charlie Nelson for letting me ciphon a small part of their electronics expertise, and the hundreds of other people that have influenced me in the past few years (but for one reason or another I can't remember their names).

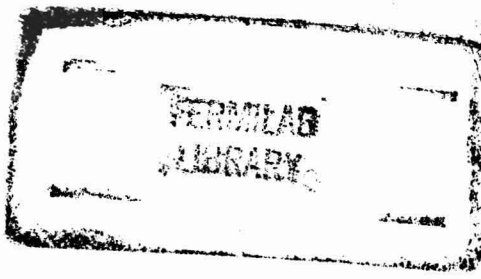

TABLE OF CONTENTS

Page

LIST OF TABLES v

LIST OF FIGURES vi

ABSTRACT viii

CHAPTER 1 – MOTIVATION 1

CHAPTER 2 – THE CDF EXPERIMENT 2

2.1 The Proton-Antiproton Collider 2
2.2 Overview of the CDF Detector 8
2.3 The CDF Solenoid Magnet 9
2.4 Central Charged Particle Tracking 12
2.4.1 Vertex Time Projection Chamber (VTPC) 12
2.4.2 Central Tracking Chamber (CTC) 14
2.5 Calorimetry 17
2.5.1 Central Electromagnetic calorimeters 17
2.5.2 Central and endwall hadron calorimeters 18
2.5.3 End plug electromagnetic shower counters 23
2.5.4 End plug hadron calorimeters 23
2.5.5 Forward electromagnetic shower counters 25
2.5.6 Forward hadron calorimeters 27
2.6 Hadron TDC 27
2.7 Central Muon Detection 28
2.8 Beam-beam Counters 30
2.8.1 Luminosity measurement 30
2.9 Jet Trigger System 31
2.10 Calorimetry Front End Electronics (Rabbit) 32
2.11 Tracking Chamber Electronics 33
2.12 Data Aquisition System 33

Page

CHAPTER 3 – ANALYSIS OF JET DATA 35

3.1 Jet algorithm 35
3.2 Jet background cuts 36
3.3 Acceptance region and raw data sample 40
3.4 Jet energy measurement 47
3.4.1 Calorimeter corrections to jet energy 47
3.4.2 Corrections to jet energy due to clustering effects 48
3.4.3 Systematic errors in jet energy measurement 48
3.5 Resolution smearing of inclusive jet spectrum 52

CHAPTER 4 – RESULTS AND CONCLUSIONS 53

4.1 Jet E_t spectrum 53
4.2 The QCD calculation of inclusive jet cross section 54
4.3 Comparison of Jet E_t spectrum with QCD calculation 55
4.4 X_t distributions and scaling violations 55
4.5 Conclusions 56

BIBLIOGRAPHY 59

VITA 61

LIST OF TABLES

Table Page

3-3-1: Buffet_Low raw data sample. 43

3-3-2: Buffet_Medium raw data sample. 44

3-3-3: Buffet_High raw data sample. 45

3-3-4: Buffet_Burn raw data sample. 46

3-5-1: Resolution smearing corrections. 52

4-1-1: The inclusive jet cross section at $\sqrt{s}$=1.8 TeV. 53

LIST OF FIGURES

Figure		Page
2-1-1:	The Fermilab $\bar{p}$ source and collider.	4
2-1-2:	The accumulation of $\bar{p}$'s in the Accumulator.	6
2-2-1:	Isometric view of the CDF detector.	10
2-2-2:	Vertical cut through one half of the CDF detector.	11
2-3-1:	Aluminum stabilized conductor for CDF solenoid.	13
2-4-1:	Isometric view of two VTPC modules.	15
2-4-2:	End view of the Central Tracking Chamber.	16
2-5-1:	CDF Central Electromagnetic calorimeter.	19
2-5-2:	Positions of Central and Endwall Hadron calorimeters.	20
2-5-3:	Central Hadron calorimeter scintillator and waveshifter strips.	21
2-5-4:	CDF End Plug EM and Hadron calorimeters.	24
2-5-5:	Cross section of the Forward EM calorimeter chamber.	26
2-6-1:	The time response of the Central Hadron calorimeter.	29
3-2-1:	The hadron time distribution for beam-beam events.	38
3-2-2:	The time distribution for Main Ring splashes and cosmic rays.	39
3-3-1:	Jet η distribution for $\|Z\| < 10$ cm.	41

Figure Page

3-3-2: Jet cross sections for different triggers. 42

3-4-1: Fractional response of the Central Calorimeter to pions. 49

3-4-2: Calorimeter response vs. jet energy. 50

3-4-3: Systematic errors in the jet energy. 51

4-3-1: The inclusive jet cross section at $\sqrt{s} = 1.8$ TeV. 57

4-4-1: The scaled jet cross section for Cern and Tevatron data. 58

ABSTRACT

Kuhlmann, Stephen Eugene. Ph.D., Purdue University, August 1988. Inclusive Central Jet Production at $\sqrt{s} = 1.8$ TeV. Major Professor: Arthur F. Garfinkel.

Jet production at $\sqrt{s} = 1.8$ TeV has been measured in the CDF detector at the Tevatron $\bar{p}p$ Collider. Jets with transverse energies of more than 200 GeV have been observed, and with a fall in cross section of about five orders of magnitude from 30 GeV to 200 GeV E_t, the observed jets provide a good testing ground for QCD. The CDF detector is a multi-purpose detector, with nearly 4π coverage of electromagnetic and hadronic calorimetry. The inclusive jet E_t production cross section was measured in the central scintillator-based calorimetry. In addition to calorimetry, the CDF detector has a central drift chamber and solenoid magnet to measure charged particle momenta, as well as a set of vertex time projection chambers to determine the event vertex position. Also, two sets of small angle scintillator counters, one on each side of the detector, provide the luminosity measurement. These detector components and their readout are described. From offline analysis of the data from these detector components, background cuts, the luminosity, the fiducial region, and the acceptance corrections have been determined, and a jet E_t spectrum was determined. Corrections to this spectrum for energy losses in the calorimetry, and smearing of the spectrum due to resolution effects are determined from Monte Carlo studies. With these corrections, the final inclusive jet production cross section $d\sigma/dE_t$ was determined, and comparisons with QCD calculations were made. Comparisons with CERN $p\bar{p}$ Collider were also made, and show the characteristics of approximate $x_t = 2p_t/\sqrt{s}$ scaling and QCD effects.

CHAPTER 1 - MOTIVATION

Whenever a new, higher energy particle accelerator is built, the popular theories of the time face new tests, and unexpected discoveries are possible that can change the direction of physics experiments and theories for years to come. Such is the case with the Fermilab Tevatron $\bar{p}p$ Collider. It produces collisions with center-of-mass energies of 1.8 TeV, almost a factor of 3 higher than the CERN $\bar{p}p$ Collider, which at 0.63 TeV had the previous highest energies. Numerous tests of the Standard Model are thus possible, encompassing electroweak theory and the present theory of the strong nuclear force, Quantum Chromodynamics (QCD). Many tests of QCD are possible at the Tevatron, most involving the study of hadronic jets. Jets are the result of hard parton scattering (either quark or gluon), and the subsequent fragmentation of the parton into a collimated jet of hadrons. QCD tests involving jets include inclusive jet measurements, angular distributions, fragmentation, multi-jet events, and many others. The lowest level 2-2 parton scattering can be predicted by QCD, and since this scattering dominates over higher order processes, good comparisons between data and theory are possible over about 5 orders of magnitude in cross section in the jet E_t distribution. In addition to the basic E_t distribution of jets, scaling violations in comparisons of CERN and Tevatron inclusive jet cross sections are expected and can be measured. These violations are a result of the Q^2 dependence of structure functions and the strong coupling constant α_s. This thesis describes the inclusive jet measurement, and subsequent comparison with QCD, as well the observance of scaling violations between CERN and Tevatron jet data.

CHAPTER 2 – THE CDF EXPERIMENT

Fermilab has built a proton-antiproton collider capable of producing CMS energies of 1.8 TeV. To study the physics at these energies, CDF has built a multi-purpose 4π detector. This detector has nearly 4π coverage of electromagnetic and hadronic calorimetry, charged particle tracking over the entire solid angle, muon coverage over the central and forward regions, and a central drift chamber and solenoid magnet to measure momenta of charged particles.

2.1 The Proton-Antiproton Collider

Fermilab has commissioned a proton-antiproton ($\bar{p}p$) collider capable of creating CMS energies of 1.8 TeV [1]. This will allow the exploration of many aspects of the Standard Model and possibly uncover many new phenomena. The bulk of the work in creating $\bar{p}p$ collisions is in making and storing the $\bar{p}$'s. The process of creating $\bar{p}$'s and storing them involves the following four steps; 1) accelerating protons to 120 GeV, then manipulating them so they have a short time distribution, 2) extracting the protons to collide with a tungsten target to create $\bar{p}$'s, 3) collecting the $\bar{p}$'s and injecting them into a synchrotron called the Debuncher, where their short time distribution is traded for a small momentum distribution, and 4) transferring the $\bar{p}$'s to a storage ring called the Accumulator where they are accumulated and stochastically cooled for several hours. Stochastic cooling is the method used to reduce the momentum distribution of the $\bar{p}$'s, as well as their transverse betatron oscillations. This will be elaborated upon in connection with its role in the Accumulator. The cycle time for $\bar{p}$ production is 2 seconds, with $\approx 10^7$ $\bar{p}$'s produced each cycle. After sufficient $\bar{p}$'s are stored, they are accelerated (along with bunches of protons) to

sufficient $\bar{p}$'s are stored, they are accelerated (along with bunches of protons) to 150 GeV in a conventional synchrotron called the Main Ring, then accelerated to 0.9 TeV and collided in a superconducting ring called the Tevatron. Figure 2-1-1 shows the relative positions of the Main Ring, Tevatron, and Accumulator.

The acceleration of protons to 120 GeV is also a multi-stage process involving several different machines. First protons from a ionized hydrogen gas source are accelerated to 750 KeV by a Cockroft-Walton electrostatic accelerator, then to 200 MeV in a linac, to 8 GeV in a "small" booster synchrotron, then to 120 GeV in the Main Ring. The Main Ring is capable of energies exceeding 400 GeV, but 120 GeV is used for the following reasons. The $\bar{p}$ cross section increases with incident proton energy, but above 150 GeV the actual production of $\bar{p}$'s rises very slowly with energy since more time is needed to accelerate protons in the Main Ring. The actual selection of 120 GeV is due to practical considerations like ease of extraction and Main Ring operating costs. After injection, the 84 proton bunches are rf manipulated so they have a short time distribution (< 1 ns). A short time distribution is desired because this time distribution is carried on by the $\bar{p}$'s after their production, and is later traded for a small energy spread. This type of manipulation is called bunch rotation and is critical in making $\bar{p}$'s and repeated (sometimes in reverse) by the Debuncher, Accumulator, and Tevatron. Consider what happens to a bunch that has a small energy spread (like the Main Ring protons) and is coasting without an rf voltage. When the rf voltage is turned on quickly the bunch begins a synchrotron oscillation. After 1/4 of a synchrotron oscillation the bunch now has a small time spread and a larger energy spread and is then extracted.

After extraction, the protons (10^{12} per pulse) are directed onto a tungsten target, producing about 10^7 $\bar{p}$'s. These $\bar{p}$'s have a large momentum spread, but about 90% have momentum between 8 GeV/c and 13 GeV/c. The $\bar{p}$'s of 8.9 GeV/c are selected by a strong focusing magnet called the lithium lens. The selected $\bar{p}$'s have a momentum spread of 3%. To accomplish this strong

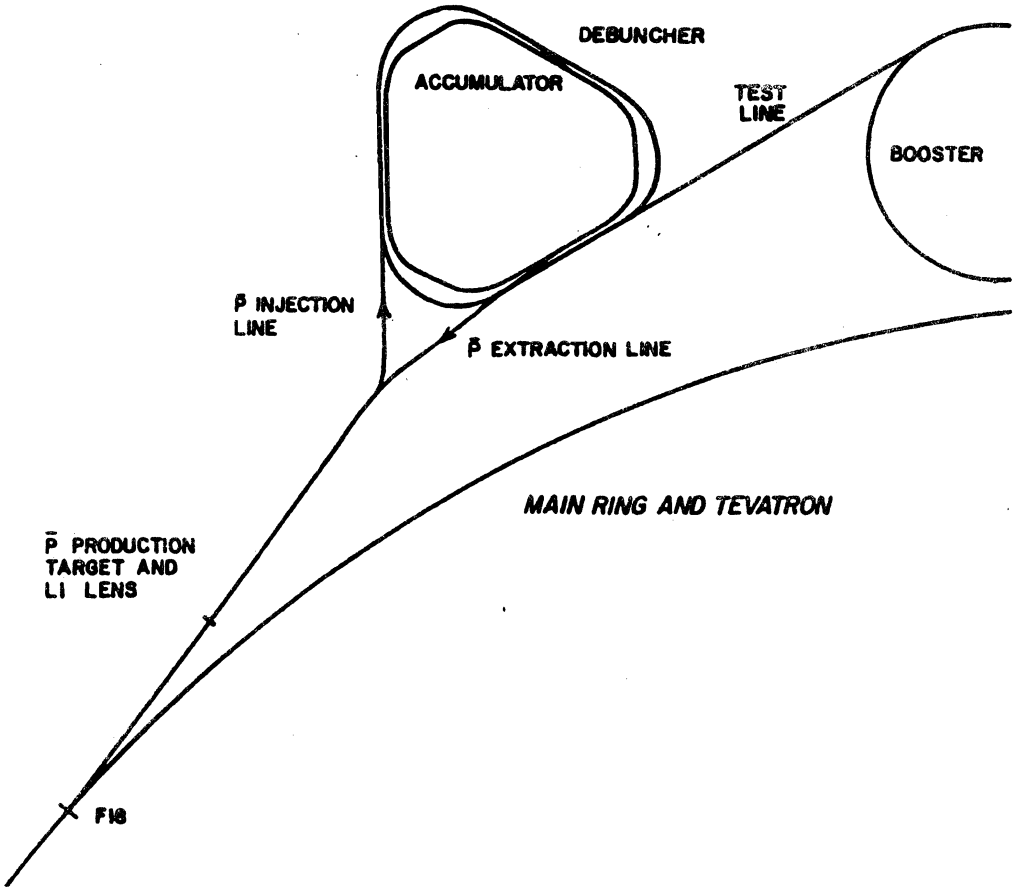

Figure 2-1-1: The Fermilab $\bar{p}$ source and collider.

focusing, the lithium lens uses a 1 MA current to produce a magnetic field gradient of 1000 T/m. The second function of the lens is to reduce the large angular divergence of the $\bar{p}$'s so they can be injected into the Debuncher. Upon exiting the lens, the transverse beam emittances (area of transverse phase space covered by the beam) are 20π mm-mrad in each plane.

The $\bar{p}$'s are injected into the Debuncher, where the small time spread is traded for a reduced energy spread by the reverse of the rf manipulation performed in the Main Ring on protons. Upon injection, the rf voltage is 5 MV, and the $\bar{p}$ bunch begins to rotate. After 1/4 of a synchrotron oscillation, the bunch has a momentum spread of about 0.2% and the rf voltage is quickly lowered to 120 KV which preserves this momentum spread. Finally the rf voltage is adiabatically removed so the original 80 bunches of $\bar{p}$'s become one. This entire process takes 12 ms, so the rest of the 2 second cycle time is used to stochastically cool the transverse betatron emittances from 20π mm-mrad to 7π mm-mrad.

When the $\bar{p}$'s are injected into the Accumulator, they are immediately rf deccelerated into a different (smaller) orbit. Then they are stochastically cooled. Consider the cooling of the transverse betatron oscillations in the vertical plane. To reduce these oscillations, beam sensors are installed above and below the beam pipe, with the difference of the signals amplified and sent across the ring to kicker electrodes, timed so that when the beam reaches the kicker electrodes it will be adjusted appropriately. So if the beam is (on the average) too high at the beam sensors, it will be moved lower at the kicker electrodes. In the Accumulator, the transverse betatron emittances are reduced to 2π mm-mmrad.

Before discussing the momentum cooling system of the Accumulator, some terms need to be defined [1]. The stacking (accumulating) proceeds as in figure 2-1-2. The accumulated $\bar{p}$'s are called the stack, with the high-density gaussian region (at -60 MeV relative to the central energy) called the core. The

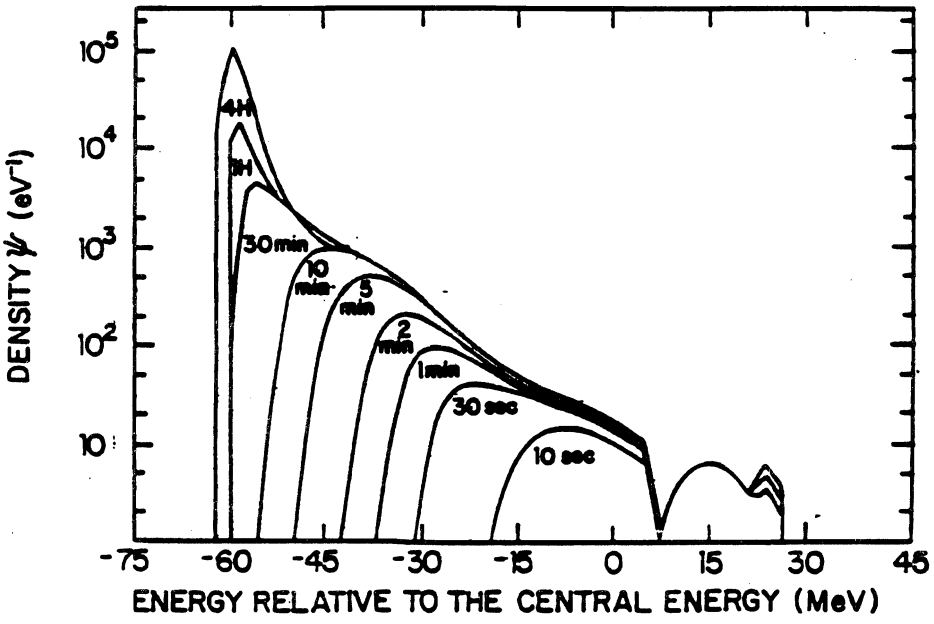

Figure 2-1-2: The accumulation of $\bar{p}$'s in the Accumulator.

exponential region is called the stack tail. Now consider the same beam sensors as used in the transverse betatron cooling, except the sum of the signals from the top and bottom sensors is amplified instead of the difference. This means the sensors are sensitive to the horizontal position of the beam instead of the vertical position. If these sensors are placed in a place of small horizontal betatron dispersion, then the sensors will be sensitive to the beam momentum since the beam radius changes with momentum. The amplified signals are then sent to notch filters, which provide a method of cooling $\bar{p}$'s at a certain radius. A notch filter lets all signals pass except for ones at a certain frequency. Since the revolution frequency depends on the beam radius, which depends on the beam momentum, a notch filter will only send a signal to a momentum kicker if the revolution frequency is not the nominal one. This technique is most important in the stack-tail momentum cooling system since signals from the particles in the core are also picked up by the stack-tail system. Without the notch filters, the stack-tail system would destroy the core inadvertantly. The notch filter, in combination with beam sensors sensitive to momentum, provide an effective method of reducing momentum dispersion. The momentum dispersion in the core is 0.05%. Stochastic cooling continuously moves $\bar{p}$'s from the stack tail to the core, until enough $\bar{p}$'s are accumulated. Then $\approx 3 \times 10^{10}$ $\bar{p}$'s are extracted from the core and injected into the Main Ring, to be accelerated and transfered into the Tevatron.

Once bunches of protons and antiprotons exist in the Tevatron, they must be manipulated so they collide at the center of the CDF detector. This process is called cogging. Upon injection, the protons and $\bar{p}$'s are passing each other some 200 meters from the CDF detector. This position is altered by changing the relative phase of the rf accelerating the protons and the rf accelerating the $\bar{p}$'s. Having this capability requires completely independent accelerating systems for the protons and $\bar{p}$'s. This can be accomplished by placing the several accelerating stations a distance $3\lambda/4$ from each other (λ the rf wavelength),

and advancing the phase of the succeeding station by 90°. The rf for the particles travelling in one direction will be out of phase from one station to the next, while the rf for the particles travelling in the other direction will be in phase. Since the protons and antiprotons travel in opposite directions, they can be controlled independently.

Another important function of the Tevatron in colliding protons and antiprotons is reducing the beam size at the collision points, thereby increasing the luminosity. This is accomplished by adding 8 focusing quadrupole magnets around the intersection points. The design luminosity is $L = 10^{30} cm^{-2} s^{-1}$, and is given by

$$L = \frac{f N_b N_p N_{\bar{p}}}{4\pi\sigma^2}.$$

N_p, $N_{\bar{p}}$ are the number of protons and antiprotons, f is the crossing frequency, N_b is the number of bunches, and $4\pi\sigma^2$ is the area of the proton and antiproton beams (assuming $\sigma = \sigma_x = \sigma_y$). If $N_p = N_{\bar{p}} = 6 \times 10^{10}$, $f = 47.7$ KHz, and $N_b = 3$, the required beam size is $\sigma = .06mm$. During the 1987 $\bar{p}p$ physics run[2], the luminosity from run to run fluctuated tremendously, but a steady improvement was seen week by week. Towards the end of the run, when conditions were more stable, the peak luminosity of $L = 10^{29} cm^{-2} s^{-1}$ was reached. During this stable period, the average number of protons per bunch was 5×10^{10}, while the average number of antiprotons was 1×10^{10}. There were 3 bunches during this run, and on the average the beam size was $\sigma = .075mm$. The integrated luminosity for the entire run was $33nb^{-1}$.

2.2 Overview of the CDF Detector

CDF has built a multi-purpose 4π detector to study a large number of different physics processes. Fortunately, many of the requirements placed on detector design by these processes overlap. These requirements include close to 4π solid angle coverage for charged particle tracking, electromagnetic

calorimetry, and hadron calorimetry. Fine granularity is desired in the calorimetry to discern single particles from jets, detect isolated leptons in the vicinity of jets, and provide position information of single particles and jets. A magnet is desired to determine the sign of charged particles and measure their momenta. This momentum measurement improves with smaller momenta thereby complimenting the calorimetry, and improves the rejection of backgrounds for detecting electrons. Muon detection over the 4π solid angle is also desirable. The CDF detector is an attempt to meet all of these requirements[3]. An isometric view of the detector is shown in figure 2-2-1, and a vertical cut through one half of the detector is shown in figure 2-2-2. A 3 meter diameter superconducting solenoid magnet provides a magnetic field of 1.5 T, which, in combination with the central tracking chamber, provides a momenta measurement of charged particles. Nearly 4π solid angle tracking of charged particles is provided by the vertex time projection chambers (VTPC), central tracking chamber (CTC), forward tracking chambers (FTC), and forward silicon strip detectors. The CDF detector also has full coverage of electromagnetic and hadron calorimetry, each with fine granularity. The muon detection system covers the central and forward rapidity regions.

2.3 The CDF Solenoid Magnet

The CDF central detector is designed to momentum analyze particles in the central tracking chamber (CTC), which is located in an axial magnetic field. To provide the desired momentum resolution of $\Delta P_t/P_t = 0.2\% \times P_t$ (GeV), the magnetic field inside the CTC should be 1.5 T. A solenoid magnet[4] was chosen to give a good momentum measurement of high P_t particles produced in the central region of the detector. To provide the 1.5 T field, a superconducting solenoid 3 m. in diameter and 5 m. long has been built, and it produces this field with a current of 5 kA. The coil resides in an iron flux return yoke which consists of two instrumented end walls and four flux return legs. The coil

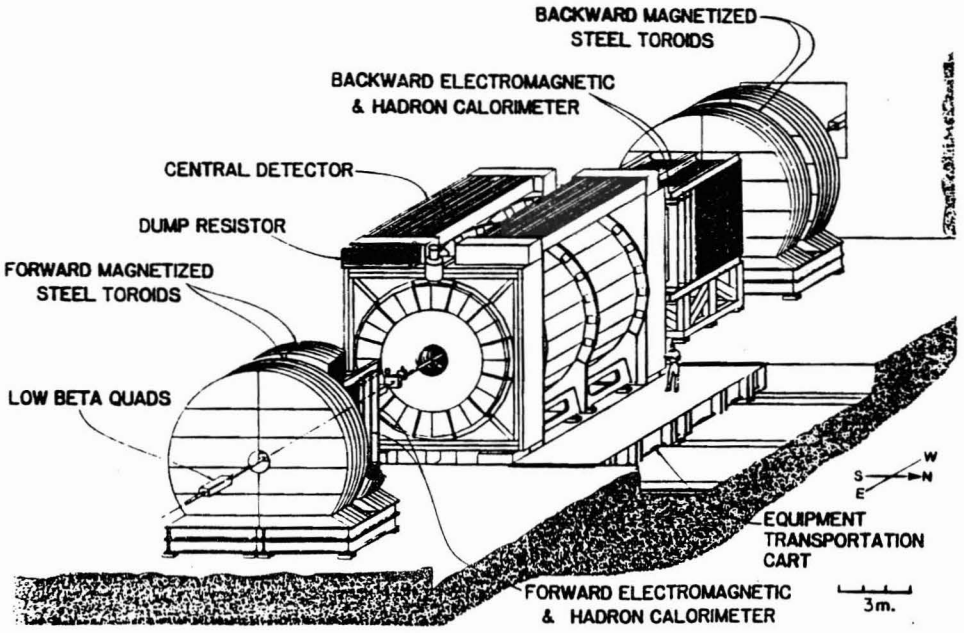

Figure 2-2-1: Isometric view of the CDF detector.

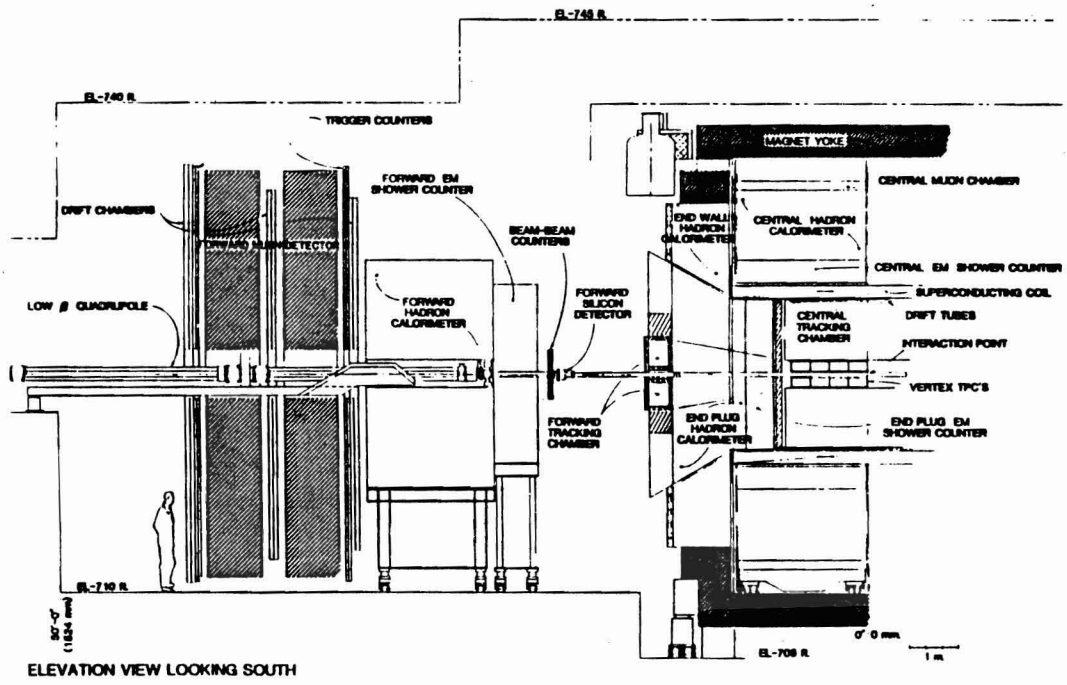

ELEVATION VIEW LOOKING SOUTH

Figure 2-2-2: Vertical cut through one half of the CDF detector.

has been kept thin (0.83 radiation lengths, 0.19 interaction lengths) since particles must pass through it before being measured by calorimetry. The superconducting wire is a copper/NbTi composite and is wound in a helical shape. As shown in figure 2-3-1, the wire is embedded in an aluminum stablizer, which not only provides construction stability, but conduction cools the wire to liquid helium temperatures (4° K).

2.4 Central Charged Particle Tracking

The main components of the CDF central tracking system are a 3 m diameter cylindrical central tracking chamber (CTC), and 8 vertex time projection chambers (VTPC). The primary goals of the central tracking systems are: 1) to measure the momentum of charged particles with good precision, and 2) to measure the position of the event vertex. With the combined VTPC and CTC system, $\approx$ 100 measurements per track will be made at 90°. The momentum resolution at 90° is $\Delta P_t/P_t = 0.2\% \times P_t$ (GeV).

Other goals of the tracking system are; to keep the drift times below the 3.5 μs between beam crossings, check for multiple interactions, and measure secondary vertices from the decay of long-lived particles. The electronics for the tracking chambers is discussed in section 2.11.

2.4.1 Vertex Time Projection Chamber (VTPC)

The VTPC[5] provides a measurement of the event vertex, which can vary by up to 100 cm. The effect of the angular difference due to the spread in event vertices is non-negligible for jet E_t measurements. The vertex is determined by searching for a common origin of the reconstructed tracks. Other uses for the VTPC include measurement of secondary vertices from the decay of long-lived particles, and to provide information about the general event topology for use in pattern recognition by the calorimetry, central tracking chamber, and forward tracking chamber.

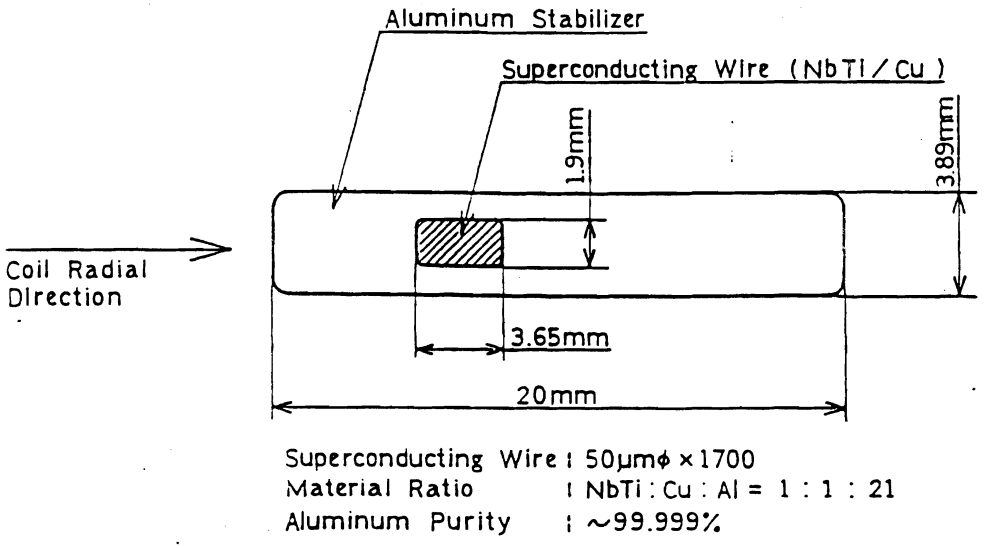

Figure 2-3-1: Aluminum stabilized conductor for CDF solenoid.

A total of 8 VTPC's are used, and are arranged along the beam pipe, centered around the collision point. Figure 2-4-1 shows two VTPC modules. A VTPC consists of two back-to-back 15 cm long drift regions which are terminated by grids backed with sense wire planes and cathode pads. The r-z coordinate of a track is measured by the drift time to one of 16 sense wires per octant. The sense wire hit times are digitized by Fastbus TDC's. The resolution in z is 200 to 350 μm depending on the drift distance.

2.4.2 Central Tracking Chamber (CTC)

The central tracking chamber[4] is an axial wire chamber positioned in the heart of the CDF central detector. The CTC can track charged particles with good efficiency in the angular region $|\eta| < 1$. Its goal is to measure the momentum of particles in conjunction with the 1.5 T magnetic field, and separate high momentum tracks inside of jets. The CTC has 84 layers of wires arranged into 9 super layers. Figure 2-4-2 shows an end view of the CTC. Five of the super layers each contain 12 sense wire planes. The other 4 super layers contain small angle stereo wires, and the two types of super layers alternate in the CTC. Each stereo layer contains 6 sense wires, all at the same stereo angle ($\pm 3°$). Both types of super layers are divided into cells so that the maximum drift time is about a microsecond. Each sense wire in the CTC is read out by a Fastbus TDC.

In the CTC, the electric field direction is $\approx 45°$ with respect to the radial direction, so the ionization electrons drift predominately in the ϕ direction when the magnetic field is 1.5 T. Tilting the cells with respect to the magnetic field helps to resolve the left/right ambiguity, since the ghost track is rotated with respect to the true track. The CTC can be used to trigger on high P_t particles, since any radial line must pass within 3.5 mm of a sense wire in each super layer. Since the drift time for 3.5 mm is about 100 ns, a coincidence between the sense wire signals in each super layer and a 100-200 ns gate (started

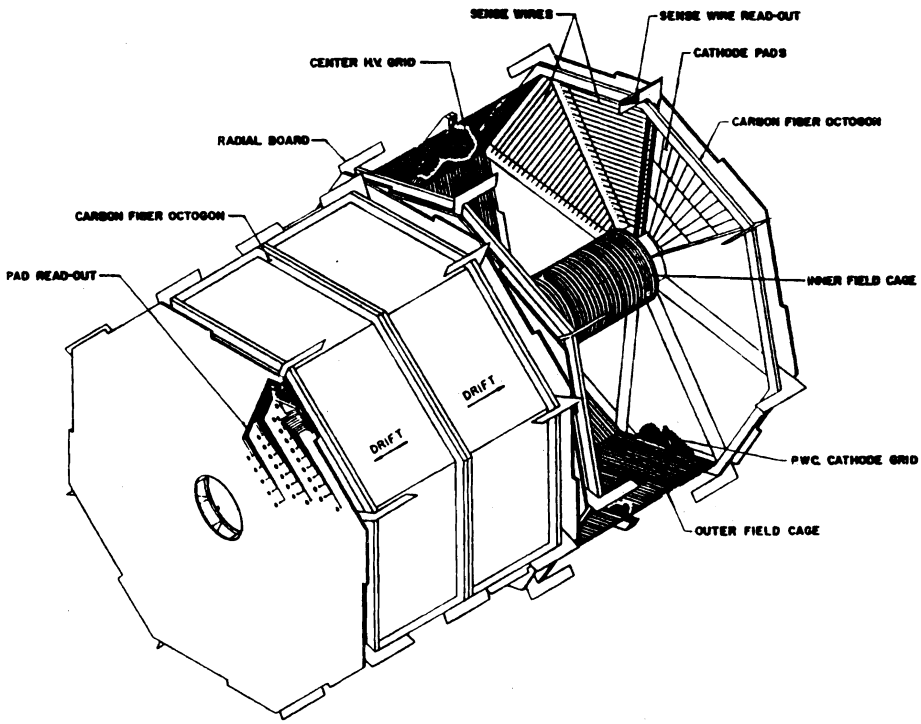

Figure 2-4-1: Isometric view of two VTPC modules.

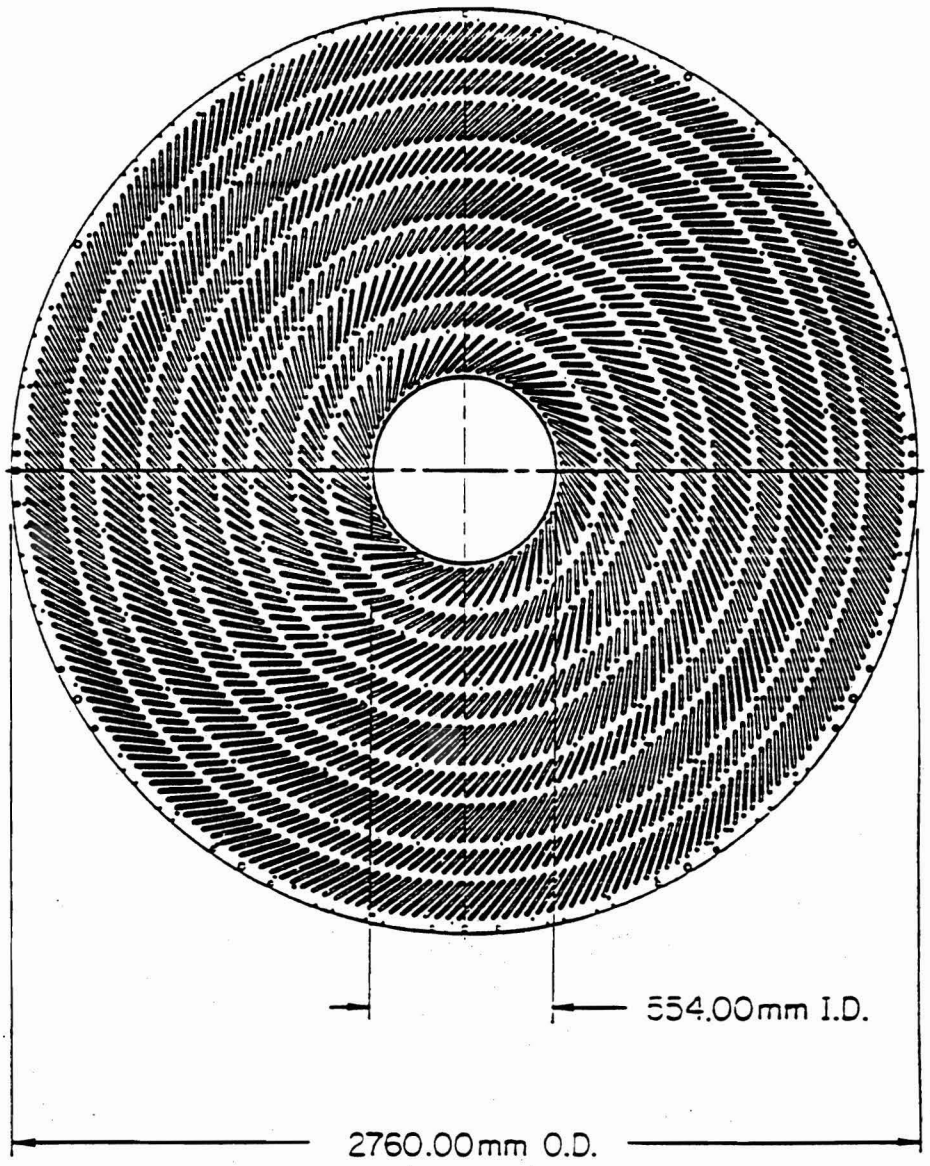

Figure 2-4-2: End view of the Central Tracking Chamber.

at the time of the beam crossing) defines a high P_t trigger. Stereo wires are used to determine the z coordinate of the track, and the resolution is about 4 mm. The stereo wires are also used to resolve the left-right ambiguity of the axial wire planes.

2.5 Calorimetry

CDF has both electromagnetic and hadronic calorimetry covering 4π in azimuth and -4.0 to 4.0 in pseudorapidity. All of the EM shower counters use lead plates to shower electrons and photons, and all of the hadron calorimeters use iron to shower hadrons. Two types of sampling media are used, scintillator in the central calorimeters and gas in the end plug and forward calorimeters. The central calorimeter is divided into 48 wedges which form a barrel surrounding the interaction point. Directly next to the central calorimeter, and on either side of it, are the end plug EM and hadron calorimeters. The endwall hadron calorimeters span the gap between the central and end plug hadron calorimeters. The forward EM shower counters and forward hadron calorimeters sit some 6.5 m from the interaction point and enclose the beam pipe. The large distance to the forward detectors is necessary for jets to spread out and to increase the distance between leptons and jets.

All of the calorimetry signals are read out by the Rabbit electronics system. This system is described in section 2.10.

2.5.1 Central Electromagnetic calorimeters

The central electromagnetic calorimeters[6] cover the angular region $|\eta| < 1.1$ and 4π in ϕ. Each wedge contains 10 towers in η of EM calorimeter. The calorimeters are a combination of shower counter and strip chamber, with the strip chamber located at shower maximum. The strip chamber gives accurate shower position, thereby helping separate photons from π^0's. The strip chambers have 128 strips and 64 wires, and its position resolution is 2 mm.

Figure 2-5-1 shows the shower counter in one wedge, with its waveshifter sheets, light guides, phototubes, and strip chamber. The shower counters have 30 layers of 1/8 in. thick lead with a layer of 5 mm. thick plastic scintillator between each lead sheet. The light from the scintillator is collected by wavelength shifters and taken to phototubes by light guides. Each tower has two phototubes, one at each extreme in phi. There are 20 radiation lengths and 1.1 absorbtion lengths total including the coil at $\eta = 0$; this increases at larger η due to the longer path length through the lead.

Each electromagnetic calorimeter was calibrated in a test beam of various energy electrons. The resolution was measured to be $14\%/\sqrt{E}$. At the time of the calibration, the response of the calorimeter was also measured with a Cs(137) gamma source. These source measurements have enabled CDF to carry over the test beam results until data is taken. The electromagnetic calorimeter phototube gains are monitored by two separate systems, a xenon flasher and a led flasher system. The light output of both systems is monitored by pin diodes.

2.5.2 Central and endwall hadron calorimeters

The central hadron calorimeters[7] cover 4π in ϕ and $|\eta| < 0.916$. Each wedge has 8 towers in η of hadron calorimeter. The endwall hadron calorimeters overlap the centrals slightly and cover $0.723 < |\eta| < 1.32$ and 4π in ϕ. Figure 2-5-2 shows the position of the central and endwall hadron calorimeters.

The central hadron calorimeters have 32 steel plates each 1 in. thick, and 1 cm. thick plastic scintillator sheets between each steel plate, giving at least 4 absorption lengths in all towers. The hadrons shower in the steel and the charged particles in the shower produce blue light in the scintillator. This light is collected by wavelength shifter bars which are placed on two sides of the scintillator. Figure 2-5-3 shows scintillator sheets and their wavelength shifter bars. The wavelength shifter is acrylic doped with laser dye #481, and

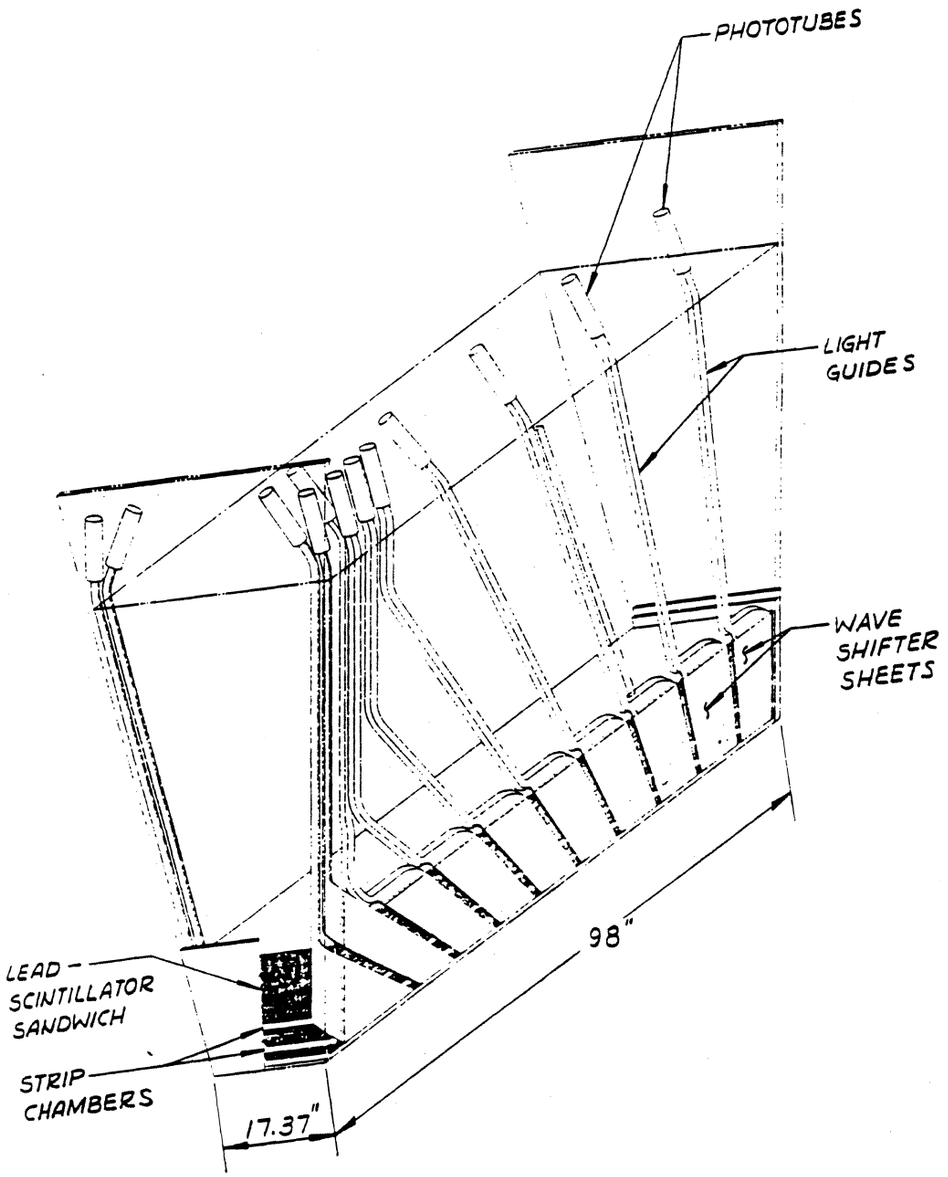

Figure 2-5-1: CDF Central Electromagnetic calorimeter.

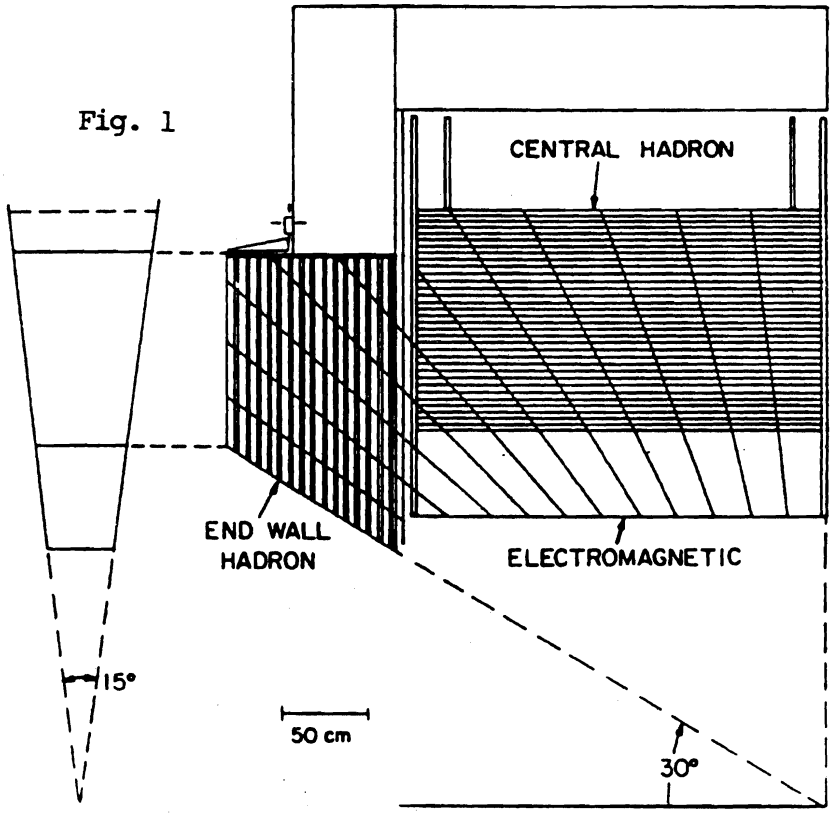

Figure 2-5-2: Positions of Central and Endwall Hadron calorimeters.

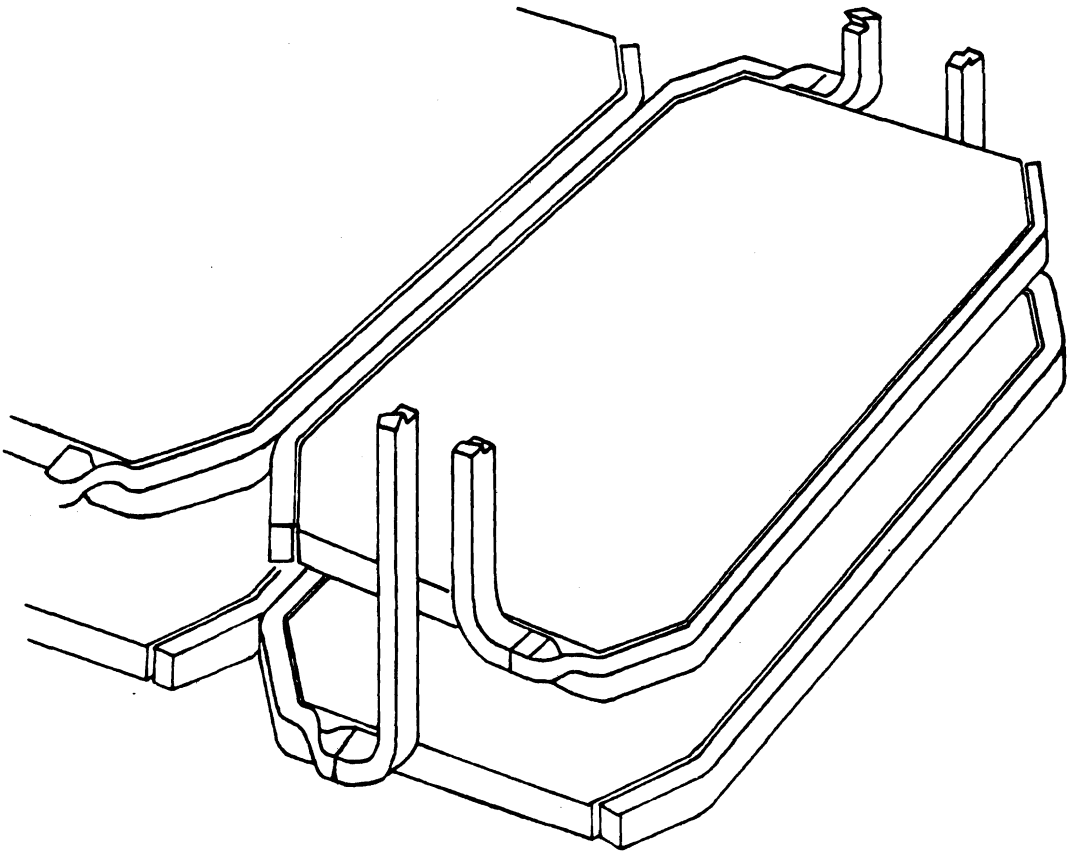

Figure 2-5-3: Central Hadron calorimeter scintillator and waveshifter strips.

emits green light isotropically after absorbing the scintillator's blue light. The wavelength shifters join smoothly onto light guides which carry the light to photomultiplier tubes, which convert the light to electrons with a gain of about 500,000. Each tower has two phototubes, one at each extreme in phi. The endwall hadron calorimeters are constructed similar to the central calorimeters, but with reduced sampling. The endwalls have 15 steel plates each 2 in. thick, with 1 cm. scintillator sheets between each plate. The response of the hadron calorimeters was measured in a test beam of various energy pions. The resolution of the central hadron calorimeter was $70\%/\sqrt{E}$ up to 50 Gev, and approximately constant at 10% from 50 Gev to 150 Gev, if the primary interaction occurs in the hadron calorimeter. If the primary interaction occurs in the electromagnetic shower counter, the resolution is $65\%/\sqrt{E}$ up to 80 Gev, and constant at 8% from 80 Gev to 150 Gev. The resolution of the endwalls was measured to be 14% at 50 Gev, which was expected due to reduced sampling.

The longitudinal response of the calorimeters was equalized by inserting filters between the wavelength shifters and the light guides, and this response was measured by running a Cs(137) gamma source longitudinally along the calorimeter.

Much effort has been made to calibrate these calorimeters. All 48 central hadron calorimeters were calibrated in a pion test beam. When the test beam calibration was performed, a parallel calibration with a Cs(137) gamma source was performed. This source is driven along one layer of scintillator, and the peak current is measured for each tower in θ. This source calibration is used to carry the test beam calibrations over to when data taking begins. In addition to the Cs(137) source, there is a separate calibration done of the phototube gains by a laser system. A nitrogen laser is pulsed electrically and the light is carried to the coupling block in front of each phototube by quartz fibers. The laser intensity is monitored by reference phototubes which also have an Americium source attached near their photocathode. The Americium is known

to be stable to better than 1%, so it acts as an absolute reference for the laser system.

2.5.3 End plug electromagnetic shower counters

The end plug electromagnetic shower counters[8] cover $1.1 < |\eta| < 2.4$ and 4π in ϕ. Figure 2-5-4 shows the end plug shower counter, with the end plug hadron calorimeter behind it. They are proportional tube gas calorimeters with 34 lead sheets as the radiator. Each layer is 90% of a radiation length. The proportional tubes are resistive plastic tubes strung with gold-plated tungsten wire. They are sandwiched inside two printed circuit boards, one of which contains ground plane while the other has the cathode pads. Each pad subtends 0.1 units of pseudorapidity and 5° in ϕ. The pads are ganged longitudinally into towers that project back to the interaction point. The pad towers have three segmentations radially, the first and last segmentations having 5 layers each while the second segmentation containing 24 layers.

The calorimeter response was measured in a test beam. The energy resolution is $24\%/\sqrt{E}$. The gas gain was monitored by proportional tubes containing radioactive sources. During data taking, the gas gain is also monitored by radioactive sources inside of proportional tubes and the various factors that contribute to gas gain changes will be monitored, like pressure and temperature.

2.5.4 End plug hadron calorimeters

Figure 2-5-4 shows the end plug hadron calorimeter[8] with the end plug electromagnetic calorimeter in front of it. The end plug hadron calorimeters cover $1.32 < |\eta| < 2.4$ and 4π in ϕ. They are proportional tube gas calorimeters with 20 layers of 2 in. steel plates intertwined with 20 layers of 1 in. proportional chambers.

The proportional chambers are very similar to the ones used in the end

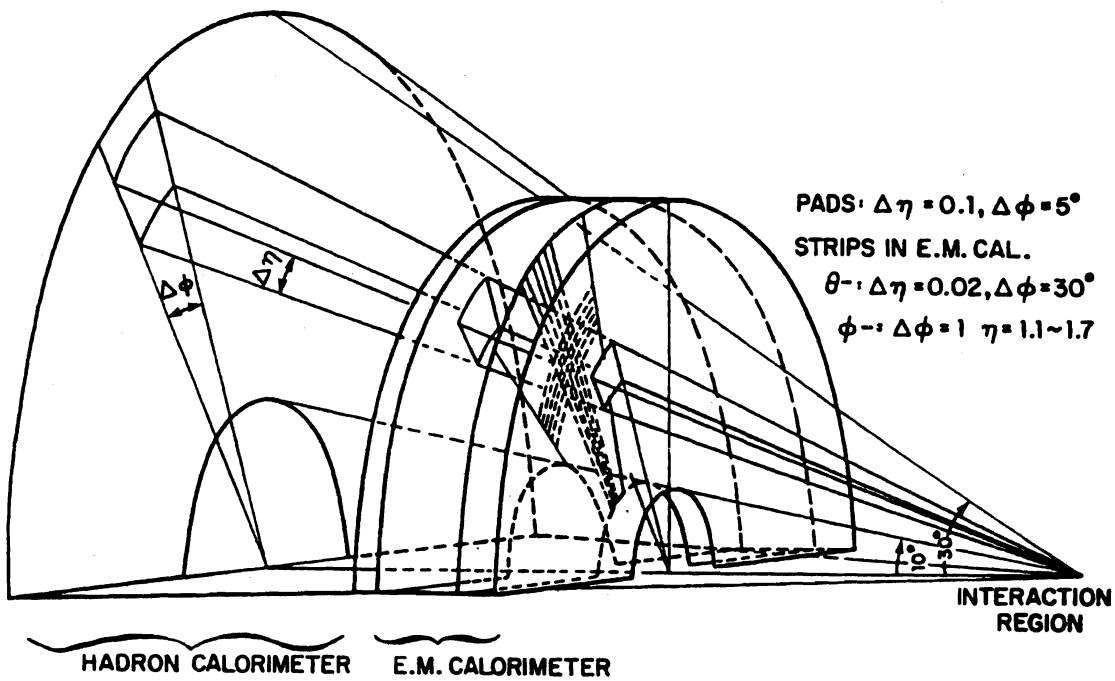

Figure 2-5-4: CDF End Plug EM and Hadron calorimeters.

plug electromagnetic calorimeters. The chambers are made of two printed circuit boards with resistive plastic tubes sandwiched in between. Inside the tubes is strung a gold-plated tungsten wire. One of the circuit boards contains ground plane, while the other has the cathode pads. Each pad subtends 0.1 units of pseudorapidity and 5° in ϕ. The pads are ganged longitudinally into towers that project back to the interaction point. The pad towers have two segmentations radially, each 10 layers deep.

The calorimeter response was measured in a test beam. The energy resolution is $110\%/\sqrt{E}$. The gas gain was monitored by radioactive sources inside proportional tubes, the same system as the end plug EM calorimeter and the forward calorimeters.

2.5.5 Forward electromagnetic shower counters

The forward EM shower counters[9] are proportional tube gas calorimeters, and cover the angular region $2.22 < |\eta| < 4.2$ and 4π in ϕ. They have 30 lead sheets as the radiator. Each layer is 90% of a radiation length. The proportional tubes have three walls of aluminum extrusion, topped with a board of G10 which contains the cathode pad readout. A cross section of a chamber is shown in figure 2-5-5. Each pad subtends 0.1 units of pseudorapidity and 5° in ϕ. The pads are ganged longitudinally into towers that project back to the interaction point. The pad towers have two segmentations radially, each 15 layers deep.

The calorimeter response was measured in a test beam. The energy resolution is $\approx$3% at 100 Gev, and varies like $1/\sqrt{E}$. The gas gain was monitored by proportional tubes containing radioactive sources. Over a period of weeks it was found that the gas monitor tubes and the calorimeter gain tracked each other to within 3%.

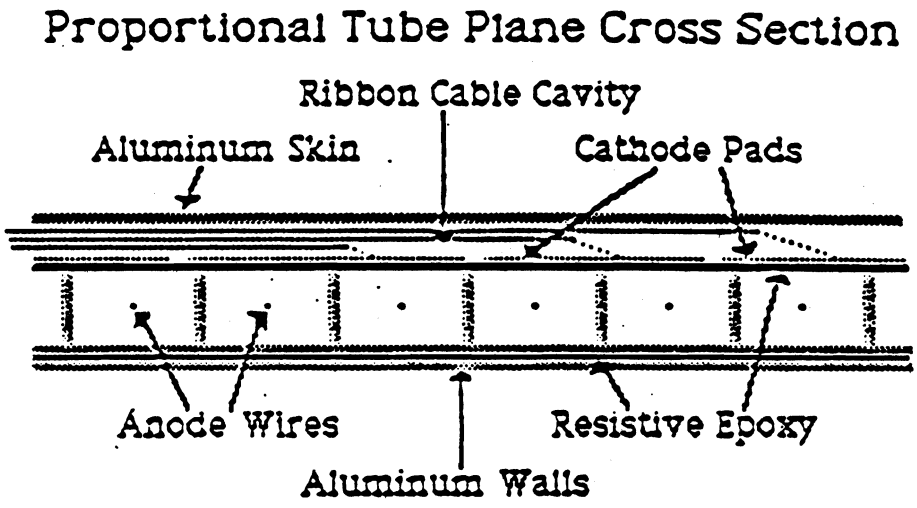

Figure 2-5-5: Cross section of the Forward EM calorimeter chamber.

2.5.6 Forward hadron calorimeters

The forward hadron calorimeters[10] are proportional tube gas calorimeters, and subtend the angular region $2.31 < |\eta| < 4.2$ and 4π in ϕ. They have 28 layers of 2 in. steel plates intertwined with 14 layers of 1 in. proportional chambers. The 28 layers of steel give 8.5 interaction lengths.

The proportional chambers are very similar to the ones used in the forward electromagnetic calorimeters. The proportional tubes have three walls of aluminum extrusion, topped with a board of G10 which contains the cathode pad readout. Each pad subtends 0.1 units of pseudorapidity and 5° in ϕ. The pads are ganged longitudinally into towers that project back to the interaction point. The pad towers have two segmentations radially, each 14 layers deep.

The calorimeter response was measured in a test beam. The energy resolution is $140\%/\sqrt{E}$. Once again, the gas gain is monitored by radioactive sources inside proportional tubes.

2.6 Hadron TDC

The central and endwall hadron calorimeters have two outputs from their phototubes, one from the anode whose signal goes to a Rabbit charge integrating amplifier, and another one from the last dynode whose signal goes to a Rabbit time-to-voltage converter card. This hadron TDC card effectively gives the time-of-flight of hadrons and muons in the hadron calorimeter.

The signals from the phototube have 10 ns rise times, and to not degrade these rise times video amplifiers are used to amplify the signal. Before further amplification by the common-base transistor amplifiers, the signals from left and right phototubes are summed. This voltage is then compared with some fixed threshold, and if over threshold the comparator fires thereby starting the TDC ramp. The ramp stops on a common stop signal, and the size of the ramp gives you the time of the signal with respect to the common stop signal. The voltage is digitized by another Rabbit card called the EWE, which is described

in section 2.10.

There are two ways of calibrating the TDC slopes, with an electronic signal whose delay can be programmed, and with the laser system used to monitor the phototube gains. Inserting long cables into the laser trigger system and using a calibrated TDC card as a reference enables the calibration of all of the TDC channels. The TDC offset, as well as the other time offsets in the hadron calorimeter, are calibrated by measuring the time of prompt collision particles. This time in combination with the known path length to the calorimeter tower provides the calibration constant.

The time response of the central and endwall hadron calorimeters was studied using a sample of about 10000 >30 GeV jet events. Figure 2-6-1 shows the wedge times with the best set of corrections and cuts. FWHM is 3 ns, which leads to a resolution of about 1.3 ns. The result of a fit to a gaussian gives a sigma of 1.38 ns, and the RMS of the distribution is 1.85 ns. There are corrections for hadron TDC channel-by-channel t0 variations, time slewing due to pulse height, event time from BBC, and path length differences from the variation of vertex position. The cuts are a 3.0 GeV cut on tower hadron energy, and a set of 2 cuts to reduce the number of anomalous early hits due to apparent energy in phi cracks. These cuts are the following: 1) Rat = (Low tube energy/High tube energy) > 0.7, and 2) Sum of the 2 neighboring phi hadron tower energies < 2.0 Gev. This set of cuts is inappropriate for some uses of the TDC, in particular in using the time-of-flight to reject jet backgrounds like cosmic rays. The use of time-of-flight in the rejection of jet backgrounds is discussed in section 4.1.

2.7 Central Muon Detection

The central muon system[11] consists of drift chambers mounted behind the central hadron calorimeters. It uses the 1.5 T magnetic field of the solenoid to measure the momenta of central muons. The drift chambers cover the

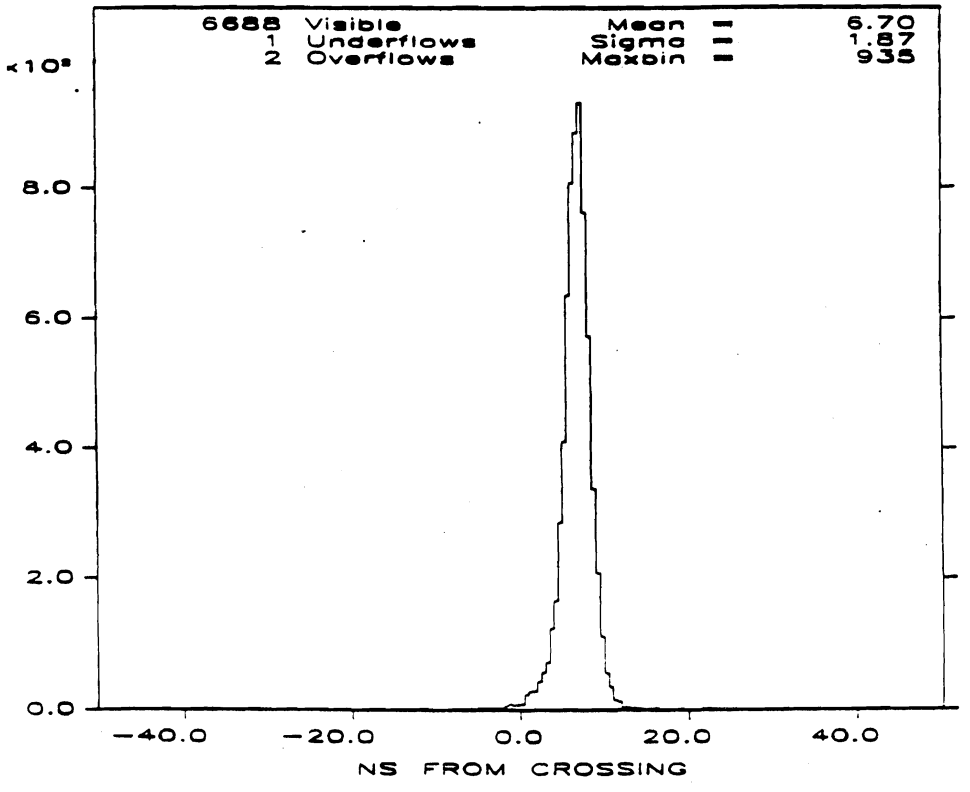

Figure 2-6-1: The time response of the Central Hadron calorimeter.

angular region $|\eta| < 0.65$ and 4π in ϕ. On each wedge there are 4 layers of wires with 12 wires on each layer. The wire signal is read out by both charge integrating amplifiers and TDC's. Charge division from the ADC's gives the z coordinate of the muon from each layer, and the TDC's give the ϕ coordinate for each layer. Using both of these gives the muon track when combining information from different layers.

A muon trigger is derived in the following way. The wires in layers 1 and 3 as well as layers 2 and 4 are aligned so they point to the interaction point. So muons with P_t greater than 5 Gev/c will give signals on the two wires with a time difference of less than 30 ns. Therefore a coincidence between the two signals provides a trigger for muons and this information is available in time for a level 1 decision. The muon chamber pulse height information, used to determine the z position of the muon, is available for the level 2 trigger.

2.8 Beam-beam Counters

The beam-beam counters are two arrays of scintillator counters, one array on each side of the central detector. They surround the beam pipe and are situated directly in front of the forward EM calorimeters. Each array has 16 counters, arranged in 4 rings of increasing diameter of 4 counters each. The counters have a measured time resolution of 200 ps, which enables them to determine the event vertex and event time with good precision. A coincidence between beam-beam counters on both sides of the detector is used in the trigger system to help ensure a beam-beam collision, as opposed to a beam gas event.

2.8.1 Luminosity measurement

The beam-beam counters are also used as a luminosity monitor. The monitor required at least a single track in each of the upstream and downstream counters. The absolute scale was set by assigning a cross section of 44.0 mb to events with charged particles in their angular range of $3.2 < \eta < 5.9$. The

value of 44.0 mb was determined from a Monte Carlo study.

2.9 Jet Trigger System

With a luminosity of $L = 10^{30} cm^{-2} s^{-1}$, there will be 75,000 collisions per second. The purpose of the trigger system[12] is to select a small fraction of interesting events to be written to tape. Some of these interesting events have well recognized signatures, but the trigger system must be versatile enough to change if new physics is found at CDF. The well recognized signatures include jets, leptons, high P_t tracks, and missing E_t.

The trigger system as designed is a three level system, but only the first level was available for the 1987 physics run. The detector elements involved in the jet trigger decision are the beam-beam counters and calorimetry. A coincidence between single tracks in each of the upstream and downstream beam-beam counters forms a minimum bias trigger, and the coincidence of a minimum bias trigger and a calorimetry summed E_t trigger forms the jet trigger.

The calorimetry trigger uses the projective geometry of the calorimeter to provide a y-ϕ map of energy flow. The signals from two adjacent towers in y are summed and form trigger towers that are coarser than detector towers. At a given y, the 24 signals giving the ϕ segmentation are shipped to Fastbus modules called receive and weight cards. These cards receive the 24 signals and adjust them for pedestal and gain. The gain includes a factor of $\sin\theta$ to convert to transverse energy. The pedestal and gain corrections are programmable through Fastbus. The signals are then sent to a second Fastbus card called the compare and sum card. Here the signals are compared to a programmable threshold and in level 1 operation, the channels over threshold are latched and their analog levels are summed to form a total E_t at a fixed value of y. The sums over y are performed by a third card called the crate sum, which also digitizes with an 8 bit flash ADC. For level 1 operation only the simple sum is

needed, and these digital results are sent to the level 1 sum box, which forms grand totals for E_t(EM), E_t(HAD), and E_t(total). The level 1 sum cards also output the results of comparisons to programmable thresholds.

The results from the level 1 sum cards, as well as the level 1 muon and beam-beam counter information go to a module called Fred, which contains the final decision logic to decide which is the trigger of the moment. The trigger decision from Fred is routed to a programmable fanout module called a crosspoint. This is used so the CDF data aquisition system may be partioned into more than one piece which can be separately triggered and read out. The trigger result from Fred is sent to the trigger supervisor for that partition, which controls the readout of the detector.

2.10 Calorimetry Front End Electronics (Rabbit)

The front end electronics system for the calorimeters is called the Rabbit system[13]. Rabbit stands for Redundant Analog Bus Based Information Transfer. The Rabbit crates are positioned on the detector, so a premium is put on reliability. That is the reason a redundant bus system is used. If one bus can not be read out, all of the electronics in the crate can be read out through the other bus. The crates are powered by redundant sets of power supplies for the same reason.

The Rabbit signals are digitized in the Rabbit crate by a module called the EWE (Event Write Encoder). The digitized signals are read out by a scanning processor called an MX, which will be discussed in section 2.12. The EWE accepts pedestals, channel addresses, and control words from the MX. The EWE selects the channel, subtracts the pedestal (if an ADC channel), tests to see if the signal is above a preset threshold, and then digitizes it. The EWE uses a 16 bit successive approximation analog to digital converter with a 17 μs conversion time.

The timing signals are generated by a card called the BAT (Before After

Timer). The BAT receives a front panel signal from the trigger system and generates all of the timing signals necessary for the front end electronics. The BAT also contains TDC's to monitor these signals, as well as power supply monitors, circuits to calibrate ADC's and TDC's, and temperature monitors.

The PM ADC card contains $\times 1$ and $\times 16$ amplifiers that integrate the charge from the photomultipliers of the central calorimetry. This card also has current channels that measure the current for cesium source calibrations.

The Hadron TDC card is discussed in detail in section 2.6.

The Muon ADC/TDC card contains both charge integrating amplifiers and TDC's. This card is used by the Central Muon chambers and the Central drift tubes. The ADC's give the z position of charged particles through charge division, while the TDC's record the drift time.

The Carrot card contains amplifiers that integrate the charge from the gas calorimetry.

The Wire card records the charge collected by the wires of the central strip chambers, while the Strip card records the charge collected by the strips of the central strip chambers.

2.11 Tracking Chamber Electronics

The tracking chamber electronics consists of ASD cards positioned in crates near the detector. This card amplifies, shapes, and discriminates (ASD) pulses from the tracking chambers. The output of this card is sent to Fastbus 1879 TDC's located in the counting room. This is a multi-hit TDC which provides both leading edge and trailing edge times of each pulse. This is useful in resolving multiple hits, and since the pulse width is related to the amount of charge collected, a measurement of the track's dE/dx can be made.

2.12 Data Acquisition System

At early stages in the data acquisition system[14] chain, there are two

distinct pipelines: 1) the calorimetry pipeline, and 2) the tracking chambers pipeline. The calorimetry pipeline begins with the digitizing cards of the Rabbit system, the EWE. The EWE is read out and controlled by a scanning processor called the MX. The MX reads the data from up to 8 Rabbit crates, buffers data from up to 4 events, and interfaces to Fastbus for upstream data processing. The tracking chambers start with digitized times in the Fastbus TDC's, which are read out by a Fastbus module called the Slac Scanner Processor (SSP).

The online computer, a Vax 11-785, receives both the calorimetry and tracking data from Fastbus through the Unibus Processor Interface (Upi). The data is formatted by a software event builder, and written to magnetic tape.

CHAPTER 3 – ANALYSIS OF JET DATA

3.1 Jet algorithm

The nature of hadronic jets, in particular the variation of fragmentation from event to event, lends itself to wide array of possible definitions of a jet. CDF has three basic jet algorithms, and has conducted a number of tests to determine the best algorithm. The three algorithms include a nearest neighbor algorithm, an E_t dependent cone algorithm, and a fixed cone algorithm. The algorithm tests include jet energy resolution, pathology searches, and multi-jet tests. Arising from these tests as the best algorithm was the fixed cone algorithm, which also has the advantage of being more directly applicable to QCD calculations.

The fixed cone algorithm has two stages, a preclustering stage and a stage where the preclusters are grown into clusters or jets. In the preclustering stage, a list of towers with $E_t > 1.0$ GeV is formed, and preclusters are defined as an unbroken chain of adjacent towers with a continuously decreasing tower E_t. If the total E_t of a precluster is larger than 2 GeV, it is used as a starting point for clustering.

In the next stage, the E_t weighted centroid of the precluster is found. Then a fixed cone in $\eta - \phi$ space of radius 0.6 is formed around the centroid, and all towers with $E_t > 200$ MeV inside this cone are merged. A new centroid is calculated from this set of towers. Again, all candidate towers inside the cone around the new centroid are merged. The process of recomputing a centroid and finding new or deleting old towers is iterated until the tower list remains unchanged.

The possibility exists that two clusters may overlap, and the handling

of these overlap conditions is important for multi-jet studies. If two clusters overlap, the E_t of the overlap region is computed and is divided by the E_t of the lower E_t cluster. If this fraction is greater than 0.5, the two clusters are merged, otherwise the towers in the overlap region are divided between the two clusters, based on the proximity of the towers to the centroid.

3.2 Jet background cuts

A substantial number of events exist where "fake" depositions of energy in the central calorimeter overlap in time with a minimum bias event and cause a jet trigger. The E_t dependence of these events is much flatter than the QCD spectrum, thus at high E_t the background dominates the signal. Thus it is important to define cuts that will efficiently remove the background events, while not cutting into the good event sample significantly. In the central hadron calorimetry, time-of-flight is the least biased and most effective tool available. But backgrounds that occur within the time window or give clusters with only em energy are missed, thus further cuts are necessary. Overall, the cuts defined in this section have proven to be very efficient in removing background events.

The first source of fake jets in the central calorimeter are spurious phototube discharges. Since each tower has two phototubes sampling the energy deposited, the ratio of the energies of the two phototubes can be used to remove these unphysical depositions. This has proven to be very efficient at all but the lowest energies, where photostatistics can sometimes give large ratios between the two phototubes.

There are two other sources of fake jets, Main Ring splashes and cosmic rays. The Main Ring is located above the central calorimetry, and beam losses can cause fake energy depositions. Cosmic ray muons can emit bremsstrahlung photons in the calorimeters, also leading to fake energy depositions. The vast majority of these jet backgrounds can be removed by cuts on the central and endwall hadron calorimeter time-of-flight. Figure 3-2-1 shows the time-of-flight

distribution for good beam-beam events, while figure 3-2-2 shows the time distribution for Main Ring and cosmic ray events.

The exact algorithm for cutting on the hadron time-of-flight is the following. The central calorimeter towers are looped over, checking for out of time hits, and summing the hadronic energy contained in the towers with out of time hits. Only TDC hits in towers with more than 1 GeV of hadronic energy are checked for whether they are in time or not. This is due to the fact that below 1 GeV the calorimeter timing degrades significantly. The time windows were selected to be -10ns<t<25ns for the central wedges and -15ns<t<55ns for the endwalls. This is where the tails of the timing distributions end for normal collisions. Towers that have more than 1 GeV in them and no TDC hit are also checked and this energy sum is also kept. The TDC is very efficient above 1 GeV, thus this is a signal of a hit in the 150 ns period where the ADC is alive but the TDC is not. If the event has 8 GeV of hadronic energy that is out of time OR the event has 8 GeV of hadronic energy in no-hits then the event is filtered.

The efficiency of the time-of-flight cuts has been studied by checking some of the other quantities that are good signs of fake jets, such as the electromagnetic fraction of the jet (EMF), the ratio of the jet's charged momenta (measured by the CTC) and the jet E_t, and the event's missing E_t. The time-of-flight cut removes > 90% of the junk events with fake jets above 70 GeV E_t, while removing only one "real" event (which appears to be a satellite bunch collision, i.e. incorrect timing). The 10% of the background missed consists of 5% in-time cosmic rays and 5% apparent cosmic rays that give all electromagnetic energy. Note that the 5% in-time cosmic rays corresponds exactly to the 35ns/700ns time window used.

The background events missed by the time-of-flight cuts are enough to distort the inclusive jet spectrum, therefore additional cuts are necessary. The additional quantities we use are those mentioned above, the electromagnetic

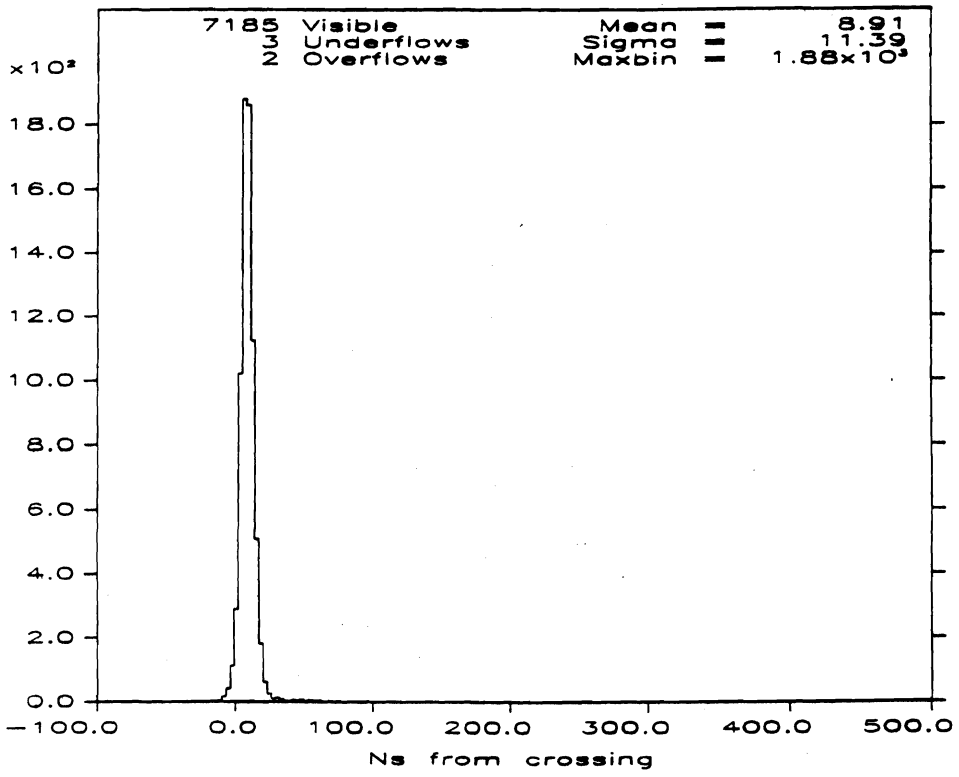

Figure 3-2-1: The hadron time distribution for beam-beam events.

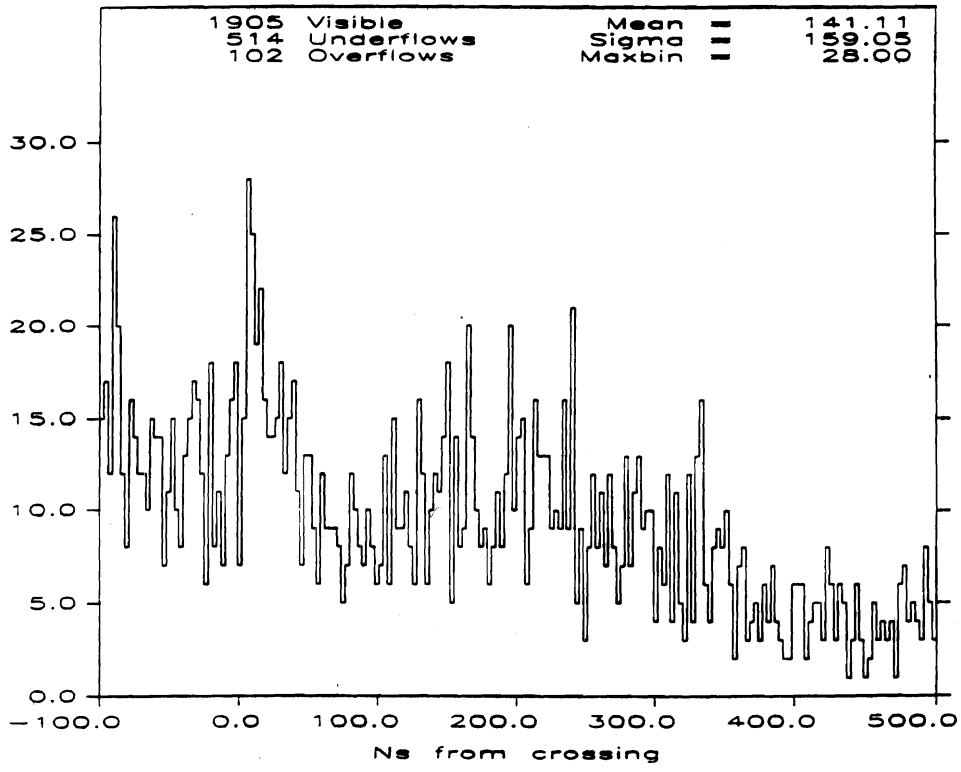

Figure 3-2-2: The time distribution for Main Ring splashes and cosmic rays.

fraction of the jet (EMF), the ratio of the jet's charged momenta (measured by the CTC) and the jet E_t, and the event's missing E_t. We flag the jet as bad if its EM fraction is outside of $0.1 < \text{EMF} < 0.95$, or if $\text{CHF} < 0.1$. For the event's missing E_t we define $0.8\sqrt{SumEt}$ as the missing E_t resolution. $SumEt$ is the scaler sum of all clusters with $E_t > 5$ GeV. Then MET = Missing $E_t/(0.8\sqrt{SumEt})$ is the "significance" of the missing E_t. MET is considered bad if MET $> 6\ \sqrt{GeV}$. The best signal to background is achieved if we require only 2 of the 3 quantities to be good. In this case all of the events kept are good, while only 4 good events (0.3%) are filtered.

3.3 Acceptance region and raw data sample

Various properties of the CDF calorimetry in the 1987 run dictate the acceptance region for jets. The CDF plug hadronic calorimeter had problems with electronic noise pickup, and was not included in the calorimetry trigger. Jets whose centroid is in or near the plug region are not triggered on efficiently, and present a problem in correcting for their acceptance when determining the inclusive jet cross section. Figure 3-3-1 shows a marked dropoff in acceptance for $\eta > 0.7$, much faster than expected from QCD. This dropoff has been confirmed to be a detector effect by checking different bands of event vertices. In addition, the CDF central calorimetry has a crack and dead region around $\eta = 0$, with significant jet energy loss and possible resolution worsening. Figure 3-3-1 also shows the drop in rate at $\eta = 0$. For these reasons, jets are only included in the inclusive jet sample if their centroid is within $0.1 < |\eta| < 0.7$. This region has full acceptance above the normal cutoff for the trigger threshold. The cutoff for each trigger threshold is determined from figure 3-3-2, and is 20 GeV for Buffet_Low, 35 GeV for Buffet_Medium, and 45 GeV for Buffet_High and Buffet_Burn.

Events whose vertex is well off-center cause additional problems. The central tracking chamber efficiency is reduced in these events, the jets enter

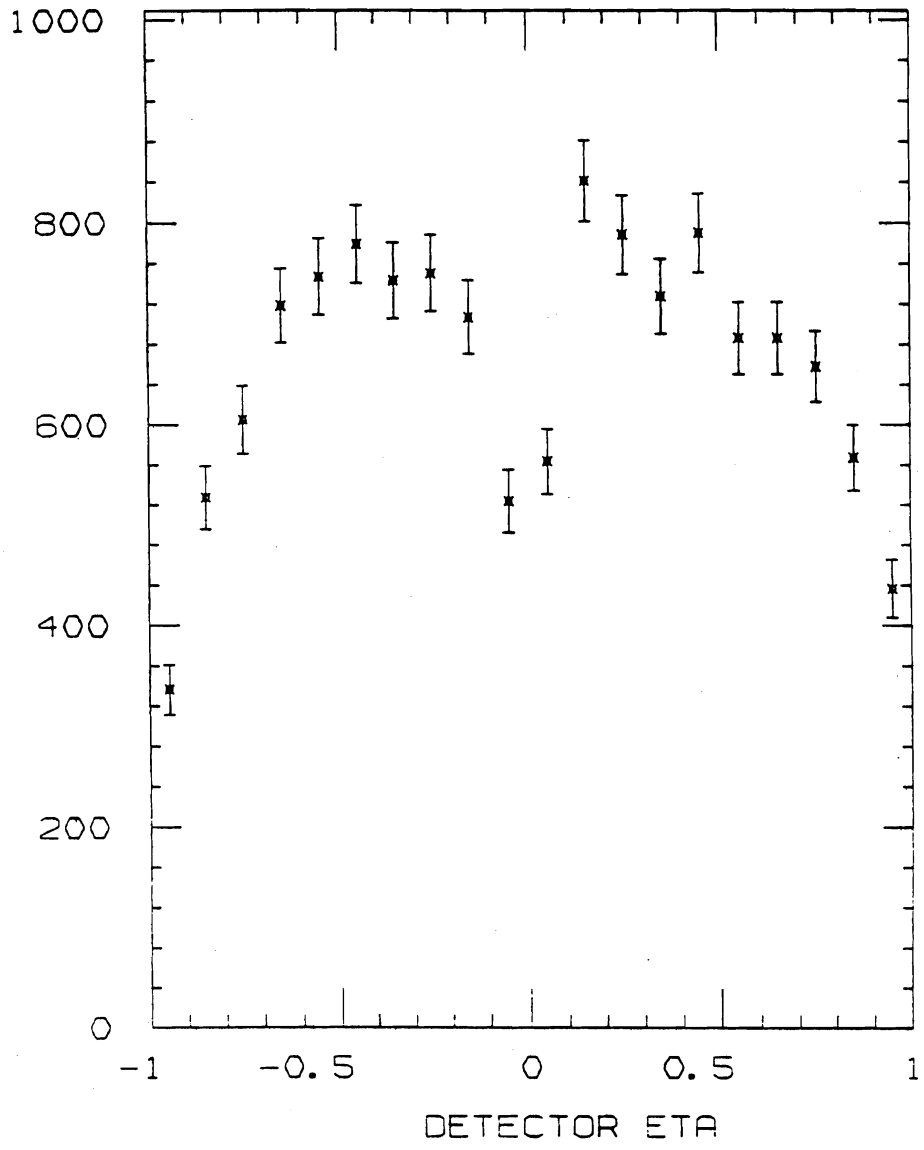

Figure 3-3-1: Jet η distribution for $|Z| < 10$ cm.

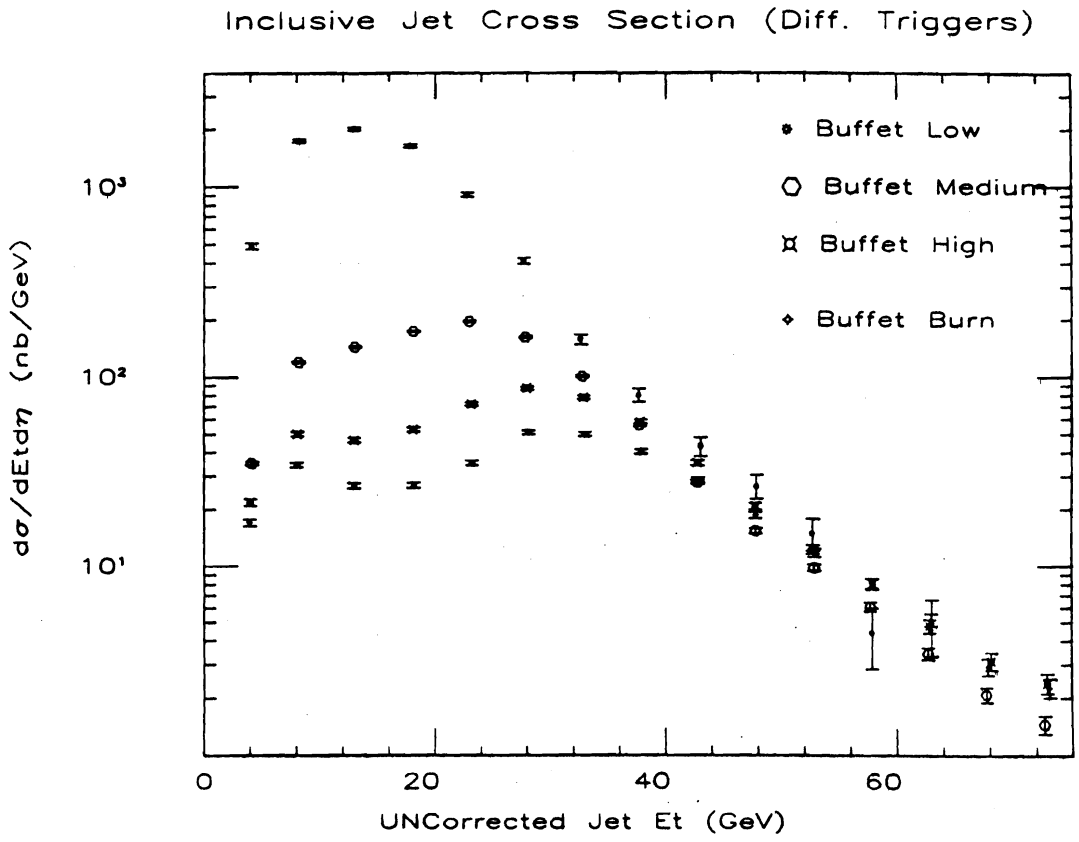

Figure 3-3-2: Jet cross sections for different triggers.

the calorimetry at unusual angles, etc. For this reason, events with a Z-vertex position of more than 60 cm from the detector center are removed, and the integrated luminosity for each run is corrected based on the Z-vertex distribution.

Using these cuts, and using the jet definition and background removal discussed earlier, we determine the sample of jets for each trigger. Table 3-3-1 shows the jet sample for the Buffet_Low triggers, table 3-3-2 is for Buffet_Medium triggers, table 3-3-3 Buffet_High triggers, and table 3-3-4 Buffet_Burn triggers.

The systematic error on the acceptance is estimated to be $< 10\%$, based on the efficiency of the acceptance region, and the uniformity of the Z-vertex distributions. This systematic error is negligible when compared with the systematic errors from the energy scale.

Table 3-3-1: Buffet_Low raw data sample.

Mean Et in 5 GeV Bin	Number of Jets	Sqrt(N)
22.18754	1038.000	31.78050
27.19905	415.0000	20.07486
32.10267	181.0000	13.26650
37.38140	98.00000	9.848858
42.21681	56.00000	7.483315
47.50148	25.00000	4.898980
51.88494	23.00000	4.690416
57.79021	9.000000	2.828427
62.99460	3.000000	1.732051
65.69437	2.000000	1.414214
71.00484	1.000000	1.000000
76.12392	2.000000	1.414214
84.86378	1.000000	1.000000
85.74632	2.000000	1.414214
94.05758	1.000000	1.000000
95.81393	1.000000	1.000000
107.1460	1.000000	1.000000
	1859	

Table 3-3-2: Buffet_Medium raw data sample.

Mean Et in 5 GeV Bin	Number of Events	Sqrt(N)
22.36591	14578.00	120.7394
27.28591	9756.000	98.77247
32.22184	5505.000	74.19569
37.19254	2782.000	52.74467
42.28585	1437.000	37.90778
47.34357	853.0000	29.20616
52.33251	484.0000	22.00000
57.25474	295.0000	17.17556
62.24317	213.0000	14.59452
67.25011	122.0000	11.04536
72.34830	87.00000	9.327379
77.40232	57.00000	7.549834
82.66984	34.00000	5.830952
87.12615	24.00000	4.898980
92.18830	13.00000	3.605551
97.19196	19.00000	4.358899
102.6691	9.000000	3.000000
107.0296	8.000000	2.828427
112.3166	7.000000	2.645751
116.8365	6.000000	2.449490
123.1387	4.000000	2.000000
126.5777	4.000000	2.000000
133.0298	7.000000	2.645751
138.4573	3.000000	1.732051
142.5875	3.000000	1.732051
151.5170	1.000000	1.000000
168.5418	2.000000	1.414214
186.9135	1.000000	1.000000
215.1581	1.000000	1.000000
	36,315	

Table 3-3-3: Buffet_High raw data sample.

Mean Et in 5 GeV Bin	Number of Events	Sqrt(N)
22.52555	2479.000	49.78956
27.40026	2353.000	48.50773
32.33294	1886.000	43.42810
37.30286	1174.000	34.26368
42.25942	711.0000	26.66458
47.26293	410.0000	20.24846
52.21640	257.0000	16.03122
57.04668	154.0000	12.40967
62.36324	86.00000	9.273619
67.27247	75.00000	8.660254
72.22240	48.00000	6.928203
77.23844	29.00000	5.385165
82.15174	24.00000	4.898980
87.81246	13.00000	3.605551
92.12746	11.00000	3.316625
97.56470	6.000000	2.449490
101.6139	4.000000	2.000000
109.4161	1.000000	1.000000
112.6640	5.000000	2.236068
127.6055	2.000000	1.414214
141.9843	1.000000	1.000000
148.1805	1.000000	1.000000
153.4920	2.000000	1.414214
170.8749	1.000000	1.000000
	9733	

Table 3-3-4: Buffet_Burn raw data sample.

Mean Et in 5 GeV Bin	Number of Events	Sqrt(N)
22.57283	1552.000	39.33192
27.46058	1792.000	42.20190
32.36087	1453.000	38.03945
37.40428	1112.000	33.31666
42.35181	700.0000	26.40076
47.35760	445.0000	21.09502
52.39307	324.0000	17.94436
57.34745	178.0000	13.30413
62.44700	114.0000	10.58300
67.07214	69.00000	8.306623
72.43011	61.00000	7.810250
77.34786	34.00000	5.830952
82.18907	28.00000	5.291502
87.55850	14.00000	3.464102
92.39343	12.00000	3.464102
97.61380	13.00000	3.605551
102.2207	8.000000	2.828427
106.3137	4.000000	2.000000
111.8413	4.000000	2.000000
117.9213	3.000000	1.732051
121.1238	1.000000	1.000000
127.2134	1.000000	1.000000
138.0651	3.000000	1.732051
153.0914	2.000000	1.414214
156.9970	1.000000	1.000000
163.6917	1.000000	1.000000
166.9619	2.000000	1.414214
178.8110	1.000000	1.000000
	7932	

3.4 Jet energy measurement

In general the observed jet energies are not the true jet energies, a jet energy correction is necessary. We divide this correction into 2 parts, the calorimeter energy losses and the losses due to clustering effects. We determine the corrections due to calorimeter effects from an Isajet Monte Carlo+Detector Simulation study, while we determine the clustering effects from the data.

3.4.1 Calorimeter corrections to jet energy

The response of the central calorimeter has been studied with test beam electrons and pions from 10-150 GeV. The response to electrons is linear with energy, and can be extrapolated to lower energies. The hadron calorimeter response has a significant non-linearity due to the changing electromagnetic fraction of hadronic showers, and must be measured for pions with less than 10 GeV. For this reason the calorimeter response to low energy pions has been studied with isolated tracks in the central tracking chamber. Figure 3-4-1 shows the fractional response for both test beam pions and low energy isolated pions in the CTC. The corresponding tuned response of simulated pions using the CDF detector simulation CDFSIM is also shown.

The uncorrected jet energy is defined as the sum of the electromagnetic and hadron compartments for each tower associated with the jet. There are various detector effects that cause significant energy losses in a jet, including detector cracks, nonlinear calorimeter response, calorimeter leakage, and various losses due to the jet algorithm. Corrections to the jet energy were measured using the ISAJET generator and a full detector simulation CDFSIM. Numerous checks of the ISAJET jet generation were made, and the fragmentation function was tuned to agree with the CDF measured fragmentation function. Jets from 10-250 GeV were generated and simulated, and the corresponding detector energy was compared with the true jet energies. Figure 3-4-2 shows the calorimeter

response as a function of jet energy. We fit a quadratic function to the region below 70 GeV, and a linear function to the region above 70 GeV. The following correction formula are obtained:

(1) Below $E_{cal} = 70$ GeV:

$$E_{jet} = (-0.1737 \times 10^{-2})(E_{cal})^2 + 1.357E_{cal} + 1.458GeV.$$

(2) Above $E_{cal} = 70$ GeV:

$$E_{jet} = 1.115E_{cal} + 9.834GeV.$$

3.4.2 Corrections to jet energy due to clustering effects

There are three effects related to the definition of a jet that require an energy correction: 1) the extra energy gained from the underlying event, 2) energy leakage outside the cone radius, and 3) the loss of jet energy due to single tower threshold. The underlying event energy density was measured by looking at 90° with respect to the jet axis. This contributes 1.1 GeV on the average to a cone of 0.6. The energy outside the cone radius was measured by varying the cone radius, and there is 2 GeV lost outside the cone on the average. The loss due to single tower threshold was measured by varying the single tower threshold, and is 400 MeV. The combination of the three effects results in a correction of 1.2±1.4 GeV to the jet energy in addition to the corrections due to calorimeter effects discussed above.

3.4.3 Systematic errors in jet energy measurement.

The sources of systematic error in the energy correction are shown in figure 3-4-3. The overall systematic error is 13.0% at 25 GeV, and 5% at 250 GeV.

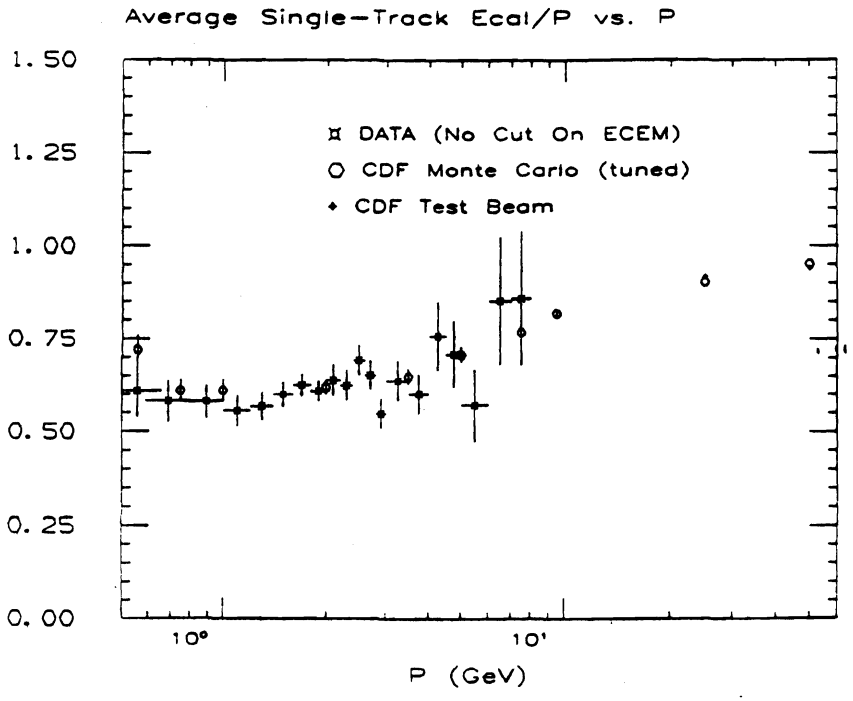

Figure 3-4-1: Fractional response of the Central Calorimeter to pions.

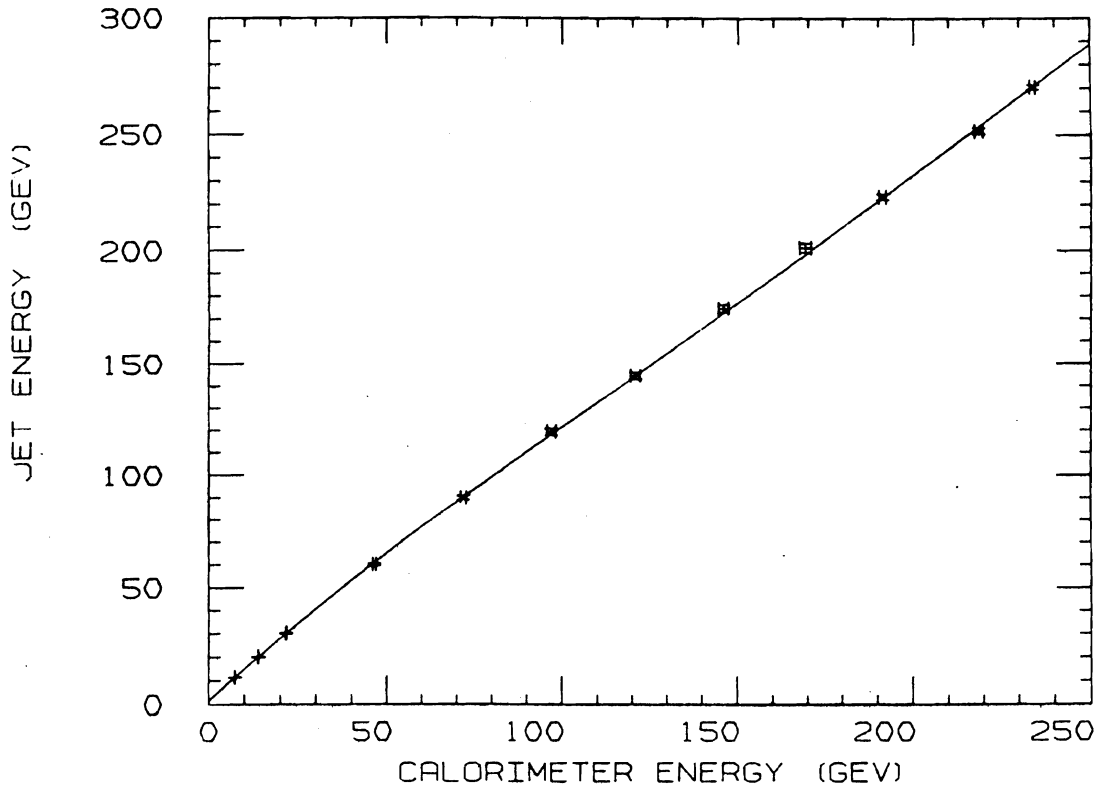

Figure 3-4-2: Calorimeter response vs. jet energy.

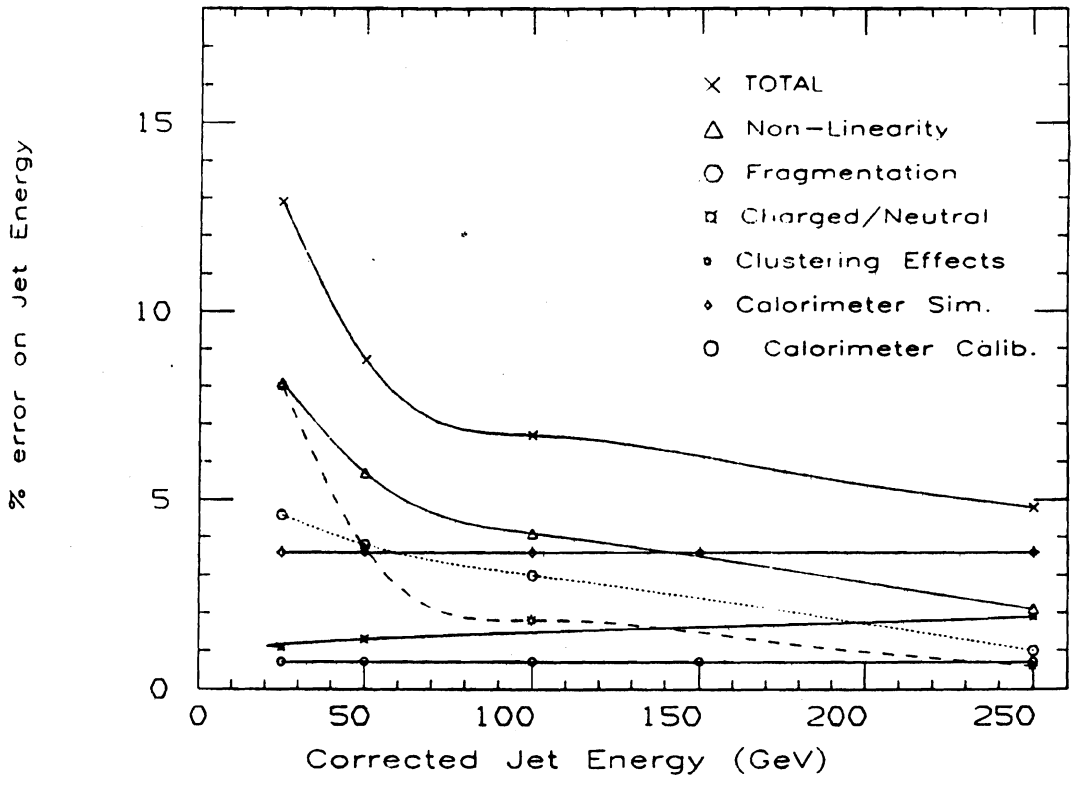

Figure 3-4-3: Systematic errors in the jet energy.

3.5 Resolution smearing of inclusive jet spectrum

The finite jet energy resolution leads to a smearing of the steeply falling inclusive jet spectrum, since jets with a certain energy that fluctuate high will fall into an E_t band with much smaller statistics. The jet energy resolution has been measured with E_t balancing techniques, and to a good approximation can be parameterized by $120\%/\sqrt{E_t}$. The smearing corrections can be measured with a simple Monte Carlo that takes an input "unsmeared" E_t distribution, smears it with the resolution function, and iterates this until the output distribution matches the data's. This has been done, and the resulting corrections to the uncorrected E_t spectrum vary from 68% at 22.5 GeV to 12% at 202.5 GeV. The systematic error on this correction has been estimated by varying the input resolution function, and is 30% at 22.5 GeV and 2% at 202.5 GeV. The corrections are given in table 3-5-1.

Table 3-5-1: Resolution smearing corrections

Jet Et	Smearing Correction	Jet Et	Smearing Correction
22.50000	1.679482	82.50000	1.230177
27.50000	1.569214	87.50000	1.220291
32.50000	1.491522	92.50000	1.211440
37.50000	1.434049	97.50000	1.203467
42.50000	1.390280	102.5000	1.196243
47.50000	1.355736	107.5000	1.189665
52.50000	1.327728	112.5000	1.183649
57.50000	1.304542	117.5000	1.178123
62.50000	1.285016	127.5000	1.168312
67.50000	1.268334	147.5000	1.152503
72.50000	1.253907	167.5000	1.140282
77.50000	1.241298	202.5000	1.124392

CHAPTER 4 – RESULTS AND CONCLUSIONS

4.1 Jet E_t spectrum

Chapter 3 defines the series of steps used to determine the inclusive jet cross section. Jets are defined by a fixed cone algorithm, and background events are removed by cuts on hadron time-of-flight, jet EM fraction, jet P_t/E_t, and missing E_t. The acceptance region is then defined as the central detector cutting out the 90° crack region, and corrections based on event vertex are made. The raw numbers of events are determined, and the corrections for luminosity and jet energy resolution are applied. Then the energy of the jet is corrected, and the cross section is divided by the rapidity interval 1.2. This leads to the inclusive jet cross section tabulated in table 4-1-1. The errors are the total errors on the cross section, statistical and systematic.

Table 4-1-1: The inclusive jet cross section at $\sqrt{s} = 1.8$ TeV.

E_t (GeV)	$d\sigma/dE_t d\eta$		E_t	$d\sigma/dE_t d\eta$	
33	230	+- 160	103	0.45	+- 0.21
39	100	+- 64	109	0.28	+- 0.13
45	44	+- 26	114	0.195	+- 0.093
52	24	+- 13	120	0.207	+- 0.098
59	12.8	+- 6.7	125	0.112	+- 0.055
64	7.6	+- 3.9	131	0.070	+ 0.040 - 0.036
70	5.0	+- 2.4	137	0.086	+ 0.046 - 0.043
76	3.0	+- 1.5	144	0.038	+ 0.021 - 0.019
81	2.01	+- 0.97	156	0.038	+ 0.021 - 0.019
87	1.33	+- 0.64	173	0.022	+ 0.011 - 0.011
92	1.00	+- 0.48	198	0.0075	+ 0.0046 - 0.0039
98	0.63	+- 0.30	236	0.0016	+ 0.0022 - 0.0012

4.2 The QCD calculation of the inclusive jet cross section

This QCD calculation of the inclusive jet cross section uses the lowest level 2-2 parton level scattering diagrams, with no corrections for gluon radiation. It takes the form of the parton probability distributions multiplied by the subprocess cross sections[15]. Equation (1) displays this form, and is the 2-jet cross section with jet 1 at rapidity y_1, and jet 2 at rapidity y_2. The inclusive jet cross section at y=0, for example, is the integral of this equation over all possible values of y_2 and y_1 set to 0.

$$\frac{d\sigma}{dp_t dy_1 dy_2} = \frac{2\pi\tau p_t}{\hat{s}} \sum_{ij} \Big\{ f^a{}_i(x_a, Q^2) f^b{}_j(x_b, Q^2) \hat{\sigma}_{ij}(\hat{s}, \hat{t}, \hat{u}) + f^a{}_j(x_a, Q^2) f^b{}_i(x_b, Q^2) \hat{\sigma}_{ij}(\hat{s}, \hat{u}, \hat{t}) \Big\} / (1 + \delta_{ij}) \tag{1}$$

The subprocess cross sections are tabulated in [15], and are given in the form $(\hat{s}/\pi)\, d\hat{\sigma}/d\hat{t}$.

$$\hat{\sigma}(q_i q_j \to q_i q_j) = \frac{4\alpha_s^2}{9\hat{s}} \frac{\hat{s}^2 + \hat{u}^2}{\hat{t}^2} \tag{2}$$

$$\hat{\sigma}(q_i \bar{q}_i \to q_j \bar{q}_j) = \frac{4\alpha_s^2}{9\hat{s}} \frac{\hat{t}^2 + \hat{u}^2}{\hat{s}^2} \tag{3}$$

$$\hat{\sigma}(q_i q_i \to q_i q_i) = \frac{4\alpha_s^2}{9\hat{u}} \left\{ \frac{\hat{t}^2 + \hat{s}^2}{\hat{u}^2} + \frac{\hat{u}^2 + \hat{s}^2}{\hat{t}^2} - \frac{2\hat{s}^2}{3\hat{u}\hat{t}} \right\} \tag{4}$$

$$\hat{\sigma}(q_i \bar{q}_i \to q_i \bar{q}_i) = \frac{4\alpha_s^2}{9\hat{s}} \left\{ \frac{\hat{t}^2 + \hat{u}^2}{\hat{s}^2} + \frac{\hat{s}^2 + \hat{u}^2}{\hat{t}^2} - \frac{2\hat{u}^2}{3\hat{s}\hat{t}} \right\} \tag{5}$$

$$\hat{\sigma}(q_i \bar{q}_i \to g g) = \frac{8\alpha_s^2(\hat{t}^2 + \hat{u}^2)}{3\hat{s}} \left\{ \frac{4}{9\hat{t}\hat{u}} - \frac{1}{\hat{s}^2} \right\} \tag{6}$$

$$\hat{\sigma}(gg \to q_i\bar{q}_i) = \frac{3\alpha_s^2(\hat{t}^2+\hat{u}^2)}{8\hat{s}}\left\{\frac{4}{9\hat{t}\hat{u}} - \frac{1}{\hat{s}^2}\right\} \tag{7}$$

$$\hat{\sigma}(gq \to gq) = \frac{\alpha_s^2(\hat{s}^2+\hat{u}^2)}{\hat{s}}\left\{\frac{1}{\hat{t}^2} - \frac{4}{9\hat{s}\hat{u}}\right\} \tag{8}$$

$$\hat{\sigma}(gg \to gg) = \frac{9\alpha_s^2}{2\hat{s}}\left\{3 - \frac{\hat{t}\hat{u}}{\hat{s}^2} - \frac{\hat{s}\hat{u}}{\hat{t}^2} - \frac{\hat{s}\hat{t}}{\hat{u}^2}\right\} \tag{9}$$

The remaining part of the calculation are the determination of parton probability distributions and the choice of scale at which to do the calculation. The parton distributions of Eichten et al.[15] are used, including both sets 1 and 2. To bracket the possible choices of scale, $Q^2 = p_t^2$ and $Q^2 = p_t^2/4$ were used. The resulting theoretical upper and lower bounds from this calculation are discussed in the following section.

4.3 Comparison of Jet E_t spectrum with QCD calculation

The variation of parton structure functions and choice of scale lead to variations between QCD calculations of the order of 50%. The measured inclusive jet cross section falls neatly inside this band of predictions. Figure 4-3-1 shows the measured distribution and the QCD calculation for EHLQ set 1 structure functions and $Q^2 = p_t^2$. The systematic errors on the data are the compilation of the systematic errors listed earlier. The errors plotted are the statistical errors and E_t dependent systematic errors. An additional systematic error of 30% on the overall normalization exists. There is generally good agreement between the data and theoretical prediction.

4.4 X_t distributions and scaling violations

The invariant jet cross section is derived from $d\sigma/dp_t$ by:

$$E\frac{d^3\sigma}{dp^3} = \frac{1}{2\pi p_t}\frac{d\sigma}{dp_t dy_1 dy_2} \tag{10}$$

By noticing the form of equation (1), the following equality is true if there is no scale dependence in the structure functions or α_s;

$$E\frac{d^3\sigma}{dp^3} = \frac{1}{p_t^4} f(x_t) \tag{11}$$

where

$$x_t = \frac{2p_t}{\sqrt{s}}. \tag{12}$$

Therefore if one plots

$$p_t^4 \; E\frac{d^3\sigma}{dp^3} = f(x_t) \tag{13}$$

for different energy regions one expects a universal curve if no scaling violations exist. However, QCD predicts scaling violations due to gluon radiation, and the plot of $f(x_t)$ is another test of QCD. Figure 4-4-1 shows the scaled jet cross sections from the Ua1 and Ua2 experiments at Cern [16], as well as the CDF data. Also shown are the QCD predictions for both 630 GeV (Cern energy) and 1800 GeV. The data from both experiments have large systematic errors, but the data suggests a scaling violation that is consistent with QCD predictions.

4.5 Conclusions

The inclusive jet cross section has been measured at CDF[17]. The measured cross section is consistent with QCD predictions. Scaling violations in x_t distributions between Cern data and our data exist, and are also consistent with QCD predictions.

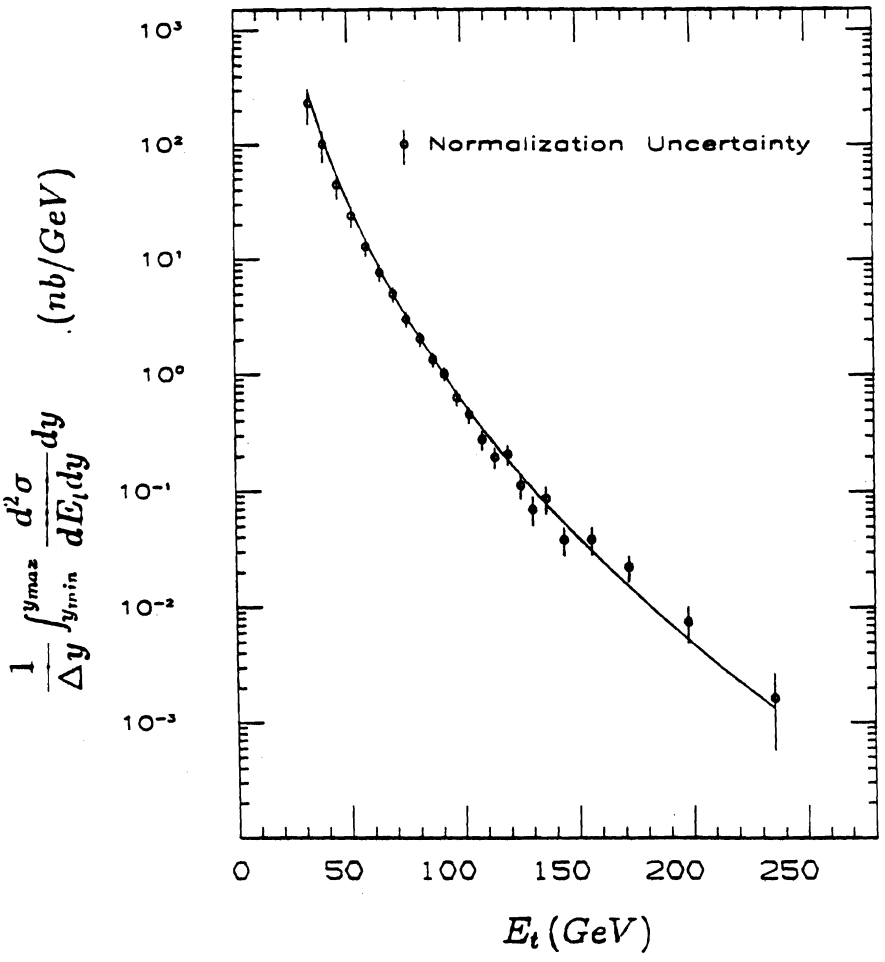

Figure 4-3-1: The inclusive jet cross section at $\sqrt{s} = 1.8$ TeV.

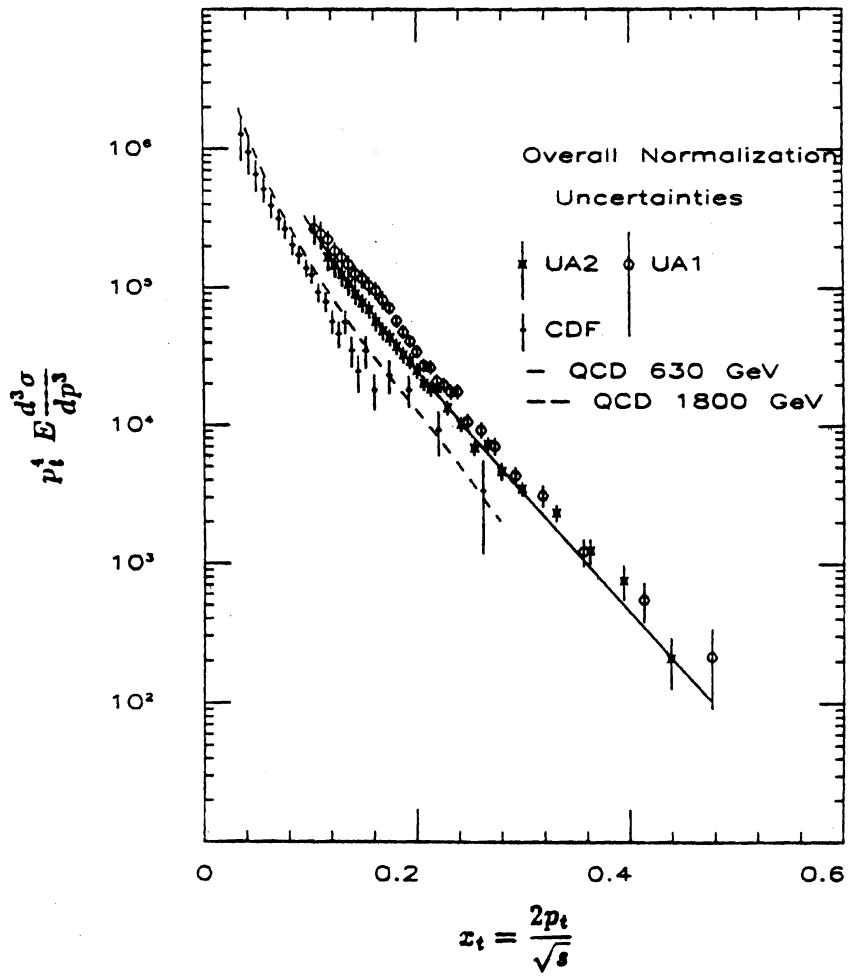

Figure 4-4-1: The scaled jet cross section for Cern and Tevatron data.

BIBLIOGRAPHY

BIBLIOGRAPHY

1. Design Report Tevatron I Project, Fermi National Accelerator Lab, Sept. 1984

2. J.L. Crawford and D.A. Finley, Fermilab Report" p. 4 (May/June, 1987)

3. "The CDF Detector: An Overview", F. Abe et al. (CDF Collaboration), Nuclear Inst. and Methods, (to be published).

4. "Design and Construction of the CDF Central Tracking Chamber", F. Bedeschi et al., Nuclear Inst. and Methods, (to be published).

5. "The CDF Vertex Time Projection Chamber System", F. Snider et al., Nuclear Inst. and Methods, (to be published).

6. "The CDF Central Electromagnetic Calorimeter", L. Balka et al., Nuclear Inst. and Methods, (to be published).

7. "The CDF Central and End Wall Hadron Calorimeter", S. Bertolucci et al., Nuclear Inst. and Methods, (to be published).

8. "The CDF End Plug Electromagnetic Calorimeter using Conductive Plastic Proportional Tubes", Y. Fukui et al., Nuclear Inst. and Methods, (to be published).

9. "An Electromagnetic Calorimeter for the Small Angle Regions of the Collider Detector at Fermilab", G. Brandenburg et al., Nuclear Inst. and Methods, (to be published).

10. "The CDF Forward/Backward Hadron Calorimeter", S. Chihangir et al., Nuclear Inst. and Methods, (to be published).

11. "CDF Central Muon Detector", G. Ascoli et al., Nuclear Inst. and Methods, (to be published).

12. "A Two Level Fastbus-Based Trigger System for CDF", D. Amidei et al., Nuclear Inst. and Methods, (to be published).

13. "CDF Front End Electronics: The RABBIT System", G. Drake et al., Nuclear Inst. and Methods, (to be published).

14. "Fastbus Data Acquisition for CDF", E. Barsotti et al., Nuclear Inst. and Methods, (to be published).

15. Eichten et al., Rev Mod. Phys. 56 (1984) 579

16. Ua1 Collab., G. Arnison et al., Phys. Lett. B 172 (1986) 461
Ua2 Collab., J.A. Appel et al., Phys. Lett. B 160 (1985) 349

17. See the following internal CDF notes for additional information:
"Performance of the Hadron Tvc Card", S. Kuhlmann et al., CDF282.
"Filtering Jet Backgrounds in the CDF Central Detector", S. Kuhlmann et al., CDF548.
"The time response of the Central and Endwall Hadron Calorimeters", S. Kuhlmann et al., CDF581.
"Clustering algorithms and their performance", D. Brown et al., CDF605.
"Steps in deriving the inclusive jet cross section", S. Kuhlmann, CDF709.
"Acceptance issues for the inclusive jet cross section", S. Kuhlmann, CDF711.
"QCD calculation of the inclusive jet cross section", J. Huth et al., CDF712.
"Response of the Central Calorimeter to Low-Energy Charged Particles", S. Behrends et al., CDF583.
"Checks of the CDFSIM central calorimeter simulation", S. Behrends et al., CDF684.
"Underlying event energy in clusters", B. Flaugher et al., CDF685.
"Central jet energy corrections due to clustering effects", S. Kuhlmann, CDF687.
"Central jet energy/momentum corrections", S. Kuhlmann et al., CDF686.

VITA

VITA

NAME — Stephen Eugene Kuhlmann

PERSONAL

[redacted]

ACADEMIC

[redacted]

Degrees:

B.S., Physics, 1982
Wichita State University

M.S., Physics, 1984
Purdue University

Ph.D., Physics, 1988
Purdue University

EMPLOYMENT EXPERIENCE

1984-Present	Research Assistant, Experimental High Energy Physics, Purdue University. Faculty advisor, Arthur Garfinkel. Thesis topic: "Inclusive Central Jet Production at $\sqrt{s} = 1.8$ TeV"
1982-1984	Teaching Assistant, Purdue University Physics Department
1980-1982	Teaching Assistant, Wichita State University Physics Department